Eindhoven University of Technology

MASTER

Fine dust production and control in a plasma jet

Ruijzendaal, M.D.

Award date:
2022

Link to publication

Disclaimer
This document contains a student thesis (bachelor's or master's), as authored by a student at Eindhoven University of Technology. Student theses are made available in the TU/e repository upon obtaining the required degree. The grade received is not published on the document as presented in the repository. The required complexity or quality of research of student theses may vary by program, and the required minimum study period may vary in duration.

General rights
Copyright and moral rights for the publications made accessible in the public portal are retained by the authors and/or other copyright owners and it is a condition of accessing publications that users recognise and abide by the legal requirements associated with these rights.

- Users may download and print one copy of any publication from the public portal for the purpose of private study or research.
- You may not further distribute the material or use it for any profit-making activity or commercial gain

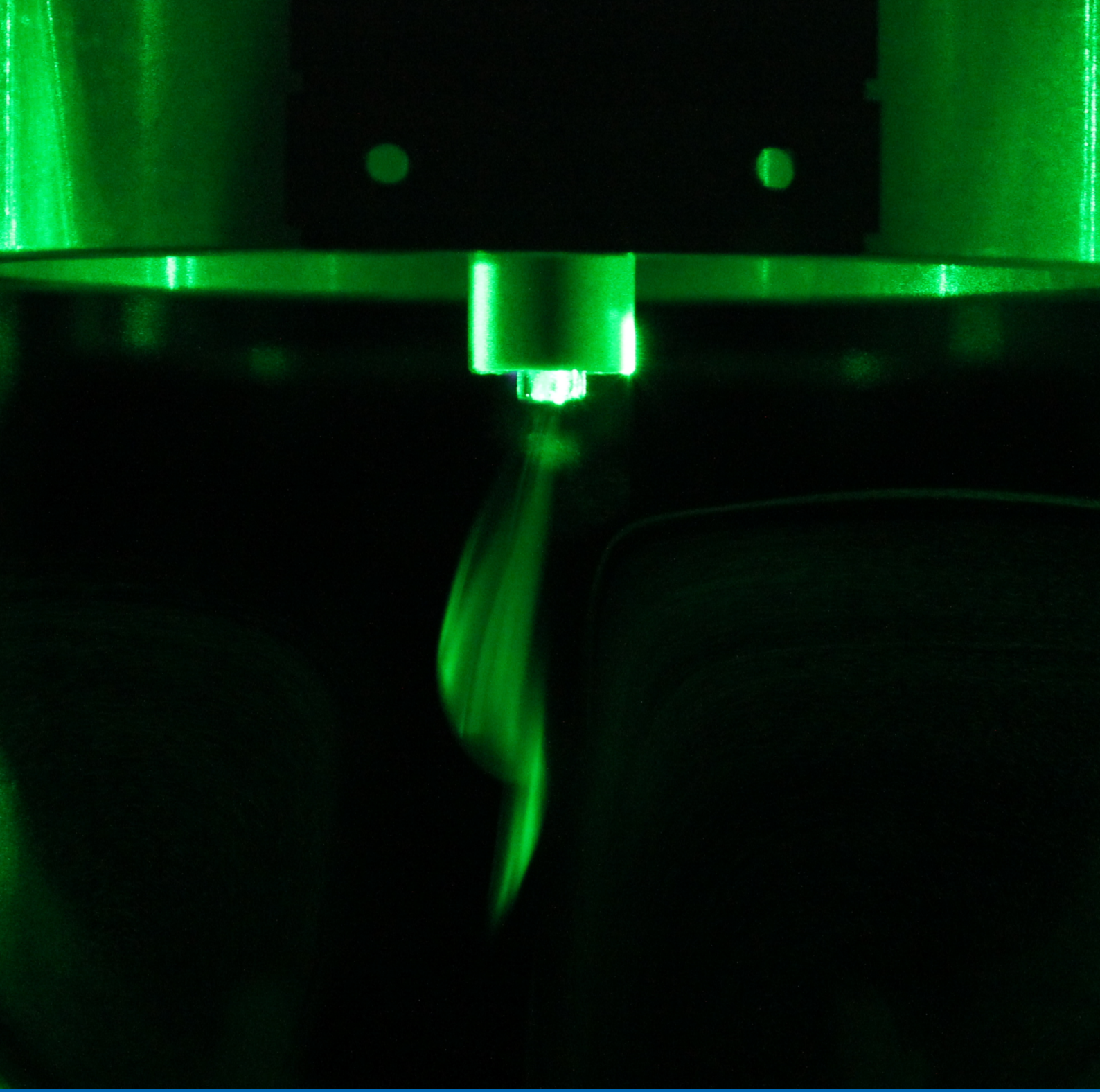

GRADUATION PROJECT

Fine dust production and control in a plasma jet

Martijn Ruijzendaal

Job Beckers	supervisor, TU/e	Niels Smith	supervisor, Prodrive Technologies
Tim Donders	supervisor, TU/e		
Tim Staps	supervisor, TU/e		

February 25^{th}, 2022

PRODRIVE TECHNOLOGIES

TU/e EINDHOVEN UNIVERSITY OF TECHNOLOGY

Fine dust production and control in a plasma jet

Martijn Daan Ruijzendaal

University	Eindhoven University of Technology (TU/e)
Department	Department of Applied Physics
Master of Science track	Plasmas and Beams
Research group	Elementary Processes in Gas Discharges (EPG)
Supervisors	ir. T.J.M. Donders ir. N. Smith (Prodrive Technologies) dr.ir. T.J.A. Staps dr.ir J. Beckers
Graduation committee	dr.ir J. Beckers (chair) dr.ir. J. van Dijk dr.ir. H.P. Huinink ir. T.J.M. Donders (advisor) dr.ir. T.J.A. Staps (advisor) ir. N. Smith (advisor)
Study load	60 ECTS (1680 hours)
Thesis submission	February 13th, 2022 (public)
Thesis defense	February 25th, 2022

The research described in this theses was carried out in accordance with the TU/e Code of Scientific Conduct.

Abstract

Next to oxygen and nitrogen, atmospheric air also contains amounts of small particles such as fine dust (PM2.5, diameter <2.5 µm) and ultrafine particles (UFP, diameter <100 nm). The health impact of these particles is increasingly studied and found to be major. The regulation of particle emission is lagging behind health research, which in turn is lagging behind the advancements made in the detection and filtering of particulate matter. This work is aimed at the development of a new production source of particulate matter. Ideally, it has controllable size density distribution so that it can be used for sensitivity and accuracy research on (ultra)fine dust sensors and filters.

The instrument of choice is a pulsed radio-frequency driven atmospheric pressure plasma jet. A reactive gas was added to the plasma, hexamethyldisiloxane (HMDSO), which is known to form spherical dust particles in the nanometer to micrometer range by polymerizing under the influence of plasma chemistry. The growth of fine dust in atmospheric plasmas currently has poor understanding, granting a challenging scientific opportunity. In this work, it was studied how the size density distribution of fine dust grown from a plasma was influenced by environmental parameters.

A method was developed for studying the size distribution of the produced fine dust. Measurements of the extinction of light in the ultraviolet-visible spectrum directed through a dust cloud were performed. The extinction spectrum is very characteristic of the size of a dust particle, which makes it possible to fit a size density distribution to the measured extinction spectrum.

Under standard experiment parameters, a particle radius mode of 104 nm was found. 50% (95%) of the observed particles was found to have a radius in the 100 to 150 nm (80 to 210 nm) range. The dust density was found to be $1.4 \times 10^{13}\,\mathrm{m}^{-3}$.

The RF pulse on-time parameter (2.5 to 20 ms) was also found to have an insignificant impact on the particle size. This can only be explained if the growth time up to 104 nm in radius is much faster than 2.5 ms, and the growth in the observed size limits is slower than 20 ms. The dust density was found to be significantly higher for increased on-times. This leads to the conclusion that there is a slow process limiting particle creation, and it is hypothesized that this is the nucleation phase in dust growth.

The plasma power parameter was scanned (11 to 24 W) but found to have no significant influence on particle size, while having a significant influence on the produced particle density. The dust density was found to have a maximum at 22 W within the power range scanned. Hypotheses of power increasing dust production and heating decreasing dust production are made.

Effective heating power on the plasma reactor through the transfer of plasma thermal energy was scanned to investigate the effects of gas temperature on dust production. As suspected in the power scan, heating was shown to have a significant effect on both size and density, but physical interpretations could not be made due to the many interfering processes.

The ratio of HMDSO admixture in the plasma flow was found to have a significant influence on power. Possible causes related to electron interactions with HMDSO molecules were outlined. The HMDSO ratio was shown to influence the power deposition per monomer, thereby having a similar effect as power: no impact on particle radius, a large impact on dust density.

This work has formed a fundamental understanding of dust growth in atmospheric pressure plasmas, and how environmental parameters can influence it. The results have shown that a plasma jet is a viable fine dust source, but further research is needed to study how particle size is influenced by the available parameters.

Based on the findings in this thesis and an extensive literature study, considerations were made on a plasma reactor concept more suited for dust growth than the setup used in this work. A radio-frequency (RF) plasma with a co-planar electrode configuration is suggested to be optimal due to homogeneity. Covering electrodes with a dielectric barrier is suggested for lifetime reasons. All factors combined, a concept schematic for an RF ring-ring plasma jet is drafted.

Table of Contents

1 Introduction

Since the industrialization, the footprint of mankind on the Earth's environment has been increasing significantly [1, 2]. The emission of CO_2 [3], chlorofluorocarbons [4], and NO_x [1, 5] all have a significant impact on the Earth's climate and the health of humans. More and more awareness of these harmful activities is raised and backed by scientists all over the world in order to prevent future emissions and, where possible, undo past emissions of harmful substances. The lifecycle of prevention iteratively passes through the process of sensing (i.e. finding the substance), impact studying (i.e. examining the influence of the substance on health or the environment), and regulation (i.e. preventing emission by law). The science and engineering of substance sensing are at the heart of every stage.

One of such harmful substances is fine dust: particles that have a diameter that is much smaller than that of a human hair (100 µm), a grain of powdered sugar (50 µm), or even a white blood cell (25 µm). Exposure to PM2.5, particulate matter smaller than 2.5 µm, has been found to significantly increase the risk of cancer, COPD, strokes, cardiovascular diseases, and many more [6–12]. Overall, all-cause mortality was found to increase by 6 % for every 10 $\mu g\,m^{-3}$ increase in P2.5 concentration [7], highlighting the importance of sensing and regulation. Sensing of PM2.5 particles is well-established, documented, and even standardized by the International Organization for Standardization (ISO) [13]. Filtering of PM2.5 is also excellent and can be performed with an efficiency of >99 % [14, 15].

More recent studies have been performed to study the impact of ultrafine particles (UFP), which have been defined as <100 nm in size [16]. These particles are so small that, upon inhalation, they can enter the bloodstream and diffuse into the brain, nervous system, and any organ [17]. Studies on health impact from UFP remain largely inconclusive [16], due to high measurement uncertainties (e.g. [18]) among other reasons. Similarly, filtering methods are not well-established, though proposals have been made [19]. It is up to science and engineering companies to challenge these issues.

Prodrive Technologies

Prodrive Technologies has a long-term commitment to environmental sensing. One of the product lines of their interest is sensors for air quality, such as the concentration of fine dust in air. Recently, Prodrive started development and manufacturing of a PM2.5 particle sensor for use in automotive air quality control [20]. The dust particles are detected using scattering of laser light, conform ISO standard [13]. During the product development, one major question arose.

All sensors have to be calibrated, i.e. the relation between an electrical signal and a physical quantity has to be known. There are a number of conventions for this calibration. First, there is Arizona road dust, which is the ISO standardized test for particulate filters [21] and is sold by the US government for a high price ($668.00 for 20 g) [22]. There is no control and no quantitative information on the size distribution of Arizona road dust. Next, there are monodisperse silica particles [23, 24] of which many properties are known. The size distribution is not controllable (unless you buy another container, that is) and they are even more expensive. Lastly, there are aerosol generators that generate particles out of a salt solution [25]. Control over the size distribution is minimal, and the operating size range might not be sufficient for all particle sensing applications.

The benefit of having more control over the size and concentration of fine dust is that the sensitivity and accuracy of a sensor, or the efficiency of a filter, can be studied far more in-depth. Dependencies on particle size and concentration can be studied, and output signal can be matched more closely to reference sensors.

For the current PM2.5 sensor and all future efforts of Prodrive Technologies on UFP sensing and filtering, the question is then,

Is there a better method for controlled production of fine dust on atmospheric pressure?

Plasma technology

It appears that the answer is *"yes"*. Within the highly reactive environment of a *plasma*, where the molecules in a gas are stripped from their electrons so that electrons and ions move around energetically, it is possible to nucleate particles and control their growth [26]. Dust growth in plasmas has historically been a complication rather than an accomplishment: it hindered high-quality thin film deposition [27–32] using plasma-enhanced chemical vapor deposition [33]. As such, research on dust growth is scarce and aimed at preventing it rather

than stimulating it. In more recent years studies have tried to stimulate and control dust growth in low-pressure plasmas [26, 34–42]. Atmospheric-pressure dust growth is gaining interest [43–46] but remains yet to be controlled.

The origin of this thesis is in this wonderful intersection of an environmental need, engineering business demand, and the scientific unknown.

Scope of this thesis

Dust formation in a plasma has been studied in literature, but never with the intention to control size or density. It is of both scientific and engineering interest to know what parameters influence the particle formation process and why. For science, formation processes can only be hypothesized once their behavior under different circumstances is measured. For engineering, it is necessary to know what parameters cause what outcome.

The goal of this graduation project, then, is to answer

- How can an atmospheric plasma be used to form fine dust?
- How can the size of the formed particles be controlled?
- How can the density of the formed particles be controlled?

Outline of this thesis

In section 2, the relevant knowledge for the work in this thesis is deconstructed. Applicable literature is quoted.

In section 3 the various diagnostic methods used to produce the results in this work are presented.

In section 4 the experimental setup used to perform the experiments for this work is introduced. The electrical and geometrical parameters are highlighted.

In section 5 the results obtained for this work are detailed. Their physical cause is hypothesized using literature.

In section 6, conclusions are drawn from the research performed for this work.

In section 7, recommendations are made for future research, based on the experiences and results found during this project.

In section 8, the relevant geometrical and electrical design parameters are studied for their influence on a fine dust-generating plasma jet. A proposal will be made as to what plasma reactor design the author thinks is best for the purpose.

2 Theory

In this section, relevant pieces from the vast knowledge on complex plasma in literature have been distilled. They will form a basis of understanding for the discussions to be had in this work.

2.1 Plasma

A brief overview of the processes playing a role in this plasma will be given here. It will be geared towards atmospheric-pressure plasma jets (APPJ's) in particular.

In popular texts a plasma is defined as the fourth state of matter, being an ionized gas. It is defined as a mixture of not only neutral molecules, but also ions and electrons. In reality, the air around the reader at this very moment is also ionized in a small amount by background radiation (e.g. presence of Potassium-40, or cosmic radiation) [47]. The difference between typical office air and a typical laboratory plasma is in the density and energy of the ions and electrons. The background radiation only leads to a very low density of electrons, whereas power is intentionally transferred to electrons in a typical laboratory plasma such that they can free additional electrons and gain high densities. A typical density of electrons n_e and ions n_i for the plasma studied in this work is 10^{20} to $10^{21}\,\mathrm{m}^{-3}$ [48, 49].

To create the plasma that is used for this work, a voltage between two electrodes is oscillated with a radiofrequency (RF) of 13.56 MHz. The electrons between the electrodes get accelerated back-and-forth, undergoing reactions with the particles they collide with. Within a steady-state of a plasma, there is a balance between the production of ions (i.e. ionization) and the loss of ions (e.g. recombination). As such, the reactions occurring in a plasma are of importance in its behavior. Typical reactions are ionization, excitation and recombination. Examples for Helium, as is used as a primary buffer gas in this work, are respectively

$$\mathrm{e} + \mathrm{He} \longrightarrow \mathrm{He}^+ + \mathrm{e} + \mathrm{e}, \tag{1}$$

$$\mathrm{e} + \mathrm{He} \longrightarrow \mathrm{He}^* + \mathrm{e}, \tag{2}$$

$$\mathrm{e} + \mathrm{He}^+ \longrightarrow \mathrm{He}^*. \tag{3}$$

Under everyday circumstances, the air surrounding us is in thermal equilibrium. The molecules in the gas constantly transfer energy between each other in such a way that the probability distribution $f(E)$ of their energy E can be described by the Boltzmann distribution that is dependent on the gas temperature $T = T_g$ as

$$f_T(E) = 2\sqrt{\frac{E}{\pi}}\left(\frac{1}{k_B T}\right)^{3/2} \exp\left(-\frac{E}{k_B T}\right), \tag{4}$$

where k_B is the Boltzmann constant. In a plasma, electrons collide very frequently with gas molecules as well, but they transfer energy less efficiently. In case of the plasma studied for this work, power is mostly absorbed by free electrons and very little of that power is transferred to the neutral gas particles via collisions. The electrons can reach temperatures T_e of 10 000 to 30 000 K (1 to 3 eV), while the gas temperature does not differ much from room temperature [50]. For this reason, the plasmas with this property are called 'cold plasmas', making them suitable for processes in treatment of industrial materials [51], food [52], and even human wounds [53].

Separation of charge, by ionization, leads to the creation of electric fields. As the charge carriers (electrons and ions) are mobile and move under the influence of electric fields, they create a shielding effect: the charge carriers arrange themselves such that any deviation in electric potential is mitigated. Under the assumption that the energy distribution of electrons in the plasma can be approximated by the Boltzmann distribution of electron temperature T_e, the length scale over which this shielding occurs is expressed as the Debye length

$$\lambda_{D_e} = \sqrt{\frac{\epsilon_0 k_B T_e}{n_e q_e^2}}, \tag{5}$$

with vacuum permittivity ϵ_0 and electron charge q_e. In an "ordinary" gas, the Debye length is very large, but a typical value of the Debye length for the plasma in this work is 1 µm.

The topic of this work is a 'complex plasma', which is a plasma that contains dust particles [54]. In this case, the dust particles will even be formed in the plasma due to complex molecular reactions. Some examples of

the reactions that can happen in molecular plasmas are dissociation, dissociative ionization and dissociative attachment, respectively

$$\mathrm{e} + \mathrm{AB} \longrightarrow \mathrm{A}^{\bullet} + \mathrm{B}^{\bullet} + \mathrm{e}, \tag{6}$$

$$\mathrm{e} + \mathrm{AB} \longrightarrow \mathrm{A}^{\bullet -} + \mathrm{B}^{\bullet +} + \mathrm{e}, \tag{7}$$

$$\mathrm{e} + \mathrm{AB} \longrightarrow \mathrm{A}^{\bullet -} + \mathrm{B}^{\bullet}. \tag{8}$$

The resulting radicals can form a variety of molecular structures which increases the complexity of the system. The rate at which reactions like these happen depends strongly on the energy of the electron, the state of the impacted particle, and the probability of the particle transitioning to a different state. The average reaction rate of a reaction A (e.g. Equation 1) can be expressed as

$$R_A = n_e n_{He} k_A = n_e n_{He} \int_0^{\infty} f_{T_e}(\epsilon) \sigma_A(\epsilon) d\epsilon, \tag{9}$$

where $\sigma_A(E)$ is the reaction cross-section.

2.2 Plasma-enhanced dust particle formation

As seen in the previous section, some molecular gases can undergo complex reactions and form molecular structures and/or solid dust particles. The gases that show this behavior are called 'precursor gases'. The precursor gas used in this work is hexamethyldisoloxane (HMDSO, $(CH_3)_3-Si-O-Si-(CH_3)_3$). Research into the synthesis of dust is performed predominantly on low pressure plasmas and predominantly on hydrocarbon and silane precursor gasses [26, 34–42]. For industrial applications on atmospheric pressure, HMDSO is often opted for due to its less volatile and less flammable characteristics compared to other precursor gasses. HMDSO comes at the cost of a more complex chemistry, as the possible combination of elements is far larger in HMDSO than e.g. ethylene. HMDSO has been widely studied in the regime where it can be used for thin film deposition. It can be used to produce scratch-resistance [55], corrosion-resistance [56] and resistance to water permeation [57]. As such, there is knowledge on HMDSO chemistry in literature.

Resulting from experiments performed on low pressure, where dust synthesis and growth is a slow process (minutes order of magnitude), a dust growth model is proposed by Bouchoule *et al.* [34]. It is depicted in Figure 2.1 and will be studied further in the subsections below. Even in modern literature on atmospheric pressure deposition and dust growth studies, this model is still used to explain dust growth. It is noted that a quantitative translation to atmospheric pressure was never made in literature, so the distinctions between the phases might differ from what will be described below.

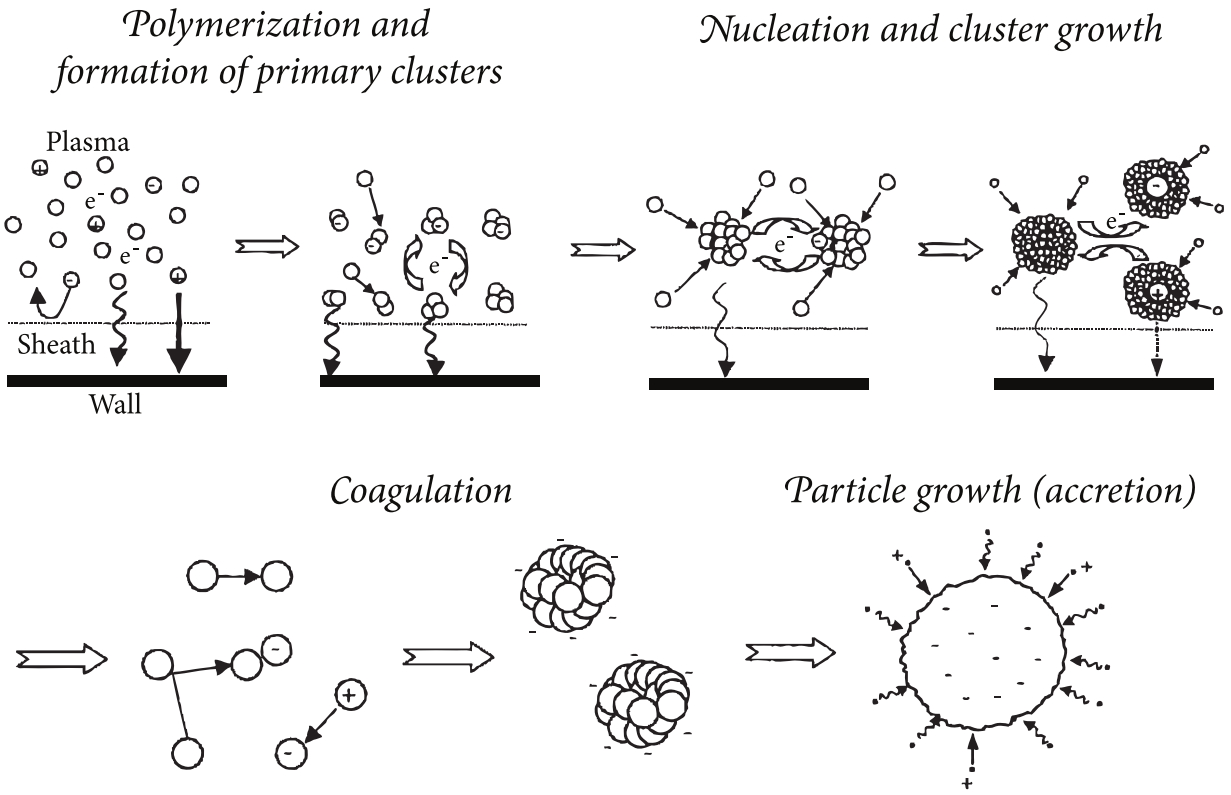

Figure 2.1: *Phases of dust growth in a plasma. Reprinted from Wetering [58], which was adapted from Bouchoule [59].*

2.2.1 Preparation

The precursor gas does not inherently form dust. When a plasma is ignited in the precursor gas, electron collisions become more frequent and more energetic. The precursor gas dissociates into smaller fragments and/or becomes ionized by electron collisions. For the purpose of this work, we define the preparation phase as starting with the gas mixture and ending with ions, radicals and monomers. This process is dominated by electron-molecule collisions ionizing and dissociating precursor molecules. On atmospheric pressure, it is therefore estimated that the processes in this phase (e.g. ionization, dissociation) cause a steady-state within a few RF cycles.

The preparation phase of dust synthesis can be fully characterized by detection of the present chemical structures (ions, radicals), which is commonly performed by mass spectrometry. A description of the species present in pure HMDSO and HMDSO plasma was done by Despax *et al.* [60]. Even without being exposed to plasma, HMDSO spontaneously dissociates into $Si_2O(CH_3)_5$ (so-called HMDSO-15) and CH_3, indicating the unstable character of the molecule. Upon exposure to plasma, HMDSO-15 is further strongly (95% reduction in concentration) dissociated into smaller fractions of mostly H_2, CH_4 and C_2H_2 neutrals [60] and complex hydrocarbon-siloxane compounds [61]. Ions originating from a HMDSO plasma show stronger fragmentation into smaller molecules [61]. As dissociation by electrons is proportional to electron density, the particles created in this phase to proceed dust formation in the next phase is largely determined by electron density and energy. Ionization cross-sections are determined by Basner *et al.* for many of these fragments, such that insight into the influence of EEDF on dissociation can be used to tune and control the species present after the preparation phase [62]. In general, reaction rates increase with increasing electron temperature as per the Arrhenius equation.

Next to electrons, there are other environmental factors effecting HMDSO. Oxygen admixture to the plasma is by far the most-discussed. Adding oxygen to the plasma appears to have a dissociative effect on the $Si-CH_3$ bonds of HMDSO [63–65], promoting fragmentation into smaller molecules and reducing carbon content in the deposited material [63].

It is important to note that the composition produced in this step determines the chemical reactions taking place in the next steps. For reference, the size of a HMDSO molecule or a fragment comparable in composition is about 1 nm.

2.2.2 Nucleation

After the preparation phase, the plasma contains a large amount of different species. Depending on the species, different growth reactions are initiated. Whereas in the preparation phase a lot of explanatory research was performed, literature in the nucleation-/polymerization phase for HMDSO is limited to descriptive research and fundamental chemistry [66]. Techniques like Fourier Transformed Infrared Spectroscopy (FTIR) and X-ray Photoelectron Spectroscopy (XPS) may be used to study chemical compositions of produced material, but they do only rarely get translated into reaction scheme propositions that are available for hydrocarbon plasmas (e.g. [67]). Nevertheless, a few conclusions can be drawn from literature.

Consensus exists in literature that an increased plasma power will cause a higher amount of fragmentation. Yasuda *et al.* define the parameter

$$Y = \frac{P}{\Phi_{mono} M_{mono}}, \tag{10}$$

with discharge power P, monomer flow rate Φ_{mono} and monomer mass M_{mono} [68]. When discussed in this work, it will be referred to as 'Yasuda parameter'. The Yasuda parameter is a measure for the amount of energy delivered to each monomer, and is used in literature as an indicator of fragmentation [64]. Fragmentation of HMDSO is exactly as discussed in subsubsection 2.2.1: dissociation and formation of carbohydrates from the monomer.

Consensus also exists about the fact that oxygen admixture in the flow lowers the carbon content of the deposited material by oxidizing into volatile molecules such as CO, CO_2, H_2O [61, 69, 70]. Friedrich suggests the following composite reaction for producing SiO_2 from an HMDSO/O_2 mixture:

$$(CH_3)_3{-}Si{-}O{-}Si{-}(CH_3)_3 + 12\,O_2 \longrightarrow 2\,SiO_2 + 6\,CO_2 + 9\,H_2O. \tag{11}$$

Working from the two earlier consensus is the following conclusion. In the high-fragmentation regime (high Yasuda parameter and/or high O_2 admixture), deposition is lower in carbon-content and more quartz(SiO_2)-like. This suggests that, in the nucleation phase, growth is dominated by reactions that form SiO_2 (amorphous) crystals.

In the low-fragmentation regime, carbon-content is higher and the structure is cross-linked monomer, similar to polydimethylsiloxane (PDMS) [63]. This indicates that growth in the nucleation phase is dominated by association of low-fragmentation radicals like HMDSO-15.

The size of nuclei developed in this step is about 5 nm. As the nuclei grow up until this size, the charge they obtain becomes influenced by the larger electron flux on their surface compared to the ion flux so that they obtain a small (a few elementary charges) net-negative charge on average.

2.2.3 Coagulation

The end of the nucleation phase is defined by the beginning of the coagulation phase, where clusters of nuclei quickly fuse together. Much literature exists on coagulation of neutral particles like aerosols [71], which is driven by thermal motion. In a plasma, particle charging and the resulting Coulombic forces play a significant role in addition to the thermal forces [35].

It is therefore of importance to describe how particles in a plasma are charged. Traditionally, Orbital Motion Limited (OML) theory is used to describe the charge a particle attains in a plasma. OML Theory solely describes thermal and Coulombic motion to determine charged particle fluxes onto the dust particle [72]. This theory, however, was developed for low-pressure plasmas and does not take into account the high collisionality of an atmospheric pressure plasma. Gatti *et al.* have developed a method combining OML theory, collisionally-enhanced, and hydrodynamic charging of dust particles [73]. Additionally, they have studied the influence of particle charge on coagulation rate.

Particles that have a charge of the same sign inhibit coagulation due to Coulombic repulsion. Even a single elementary charge will strongly inhibit coagulation between two particles [74]. At atmospheric pressure, a nanoparticle of a conservative 5 nm size will still obtain an average charge of 3 electrons when in a plasma of (conservative) $n_i = 1 \times 10^{18}\,\mathrm{m}^{-3}$ and with $n_p = 1 \times 10^{16}\,\mathrm{m}^{-3}$ [46]. The negative particle charge is balancing the high thermal electron flux relative to the low thermal ion flux. Until the nuclei density is much higher than the ion density, coagulation of nuclei will be prevented [35]. Consensus is that, when the coagulation threshold is exceeded, nuclei fuse rapidly into cauliflower-like structures.

2.2.4 Accretion

After coagulation of nuclei, the particle density has decreased drastically but the average size has increased. All particles now obtain a large negative charge and attract large ion currents. Radical collisions are also still occurring and significant. Particle size now increases at a relatively constant rate through surface growth. It is suspected that processes similar to that in the preparation and nucleation phases drive growth here.

Modeling has shown that the particle heating due to the charged particle currents can heat the particle to $>1500\,\mathrm{K}$, which may be above the crystallization temperature [46, 75]. This can transform the cauliflower structure to spherical crystals.

3 Methods

For this work, the particle size distribution is of specific interest. Listed below are the various diagnostics used in the experiments for this work to uncover information on the plasma and dust growth therein.

3.1 UV-Vis Extinction Spectroscopy

Description

The dust produced in reactive plasmas can reach high optical densities. For the particle diameters typically expected to be produced (1 to 1000 nm), refraction and absorption of visible light by the (assumed spherical) particles is best described by Mie theory [76]. Information can be obtained from the interaction of light with dust, because it is highly dependent on particle diameter, morphology and material.

The combined effect of absorbance and scattering is called extinction. Ultraviolet-visible (UV-Vis) extinction spectroscopy is the act of measuring the attenuation $\mu(\lambda)$ of an initial intensity spectrum $I_0(\lambda)$ when it is transmitted through a cloud of dust of length L along the beam path, described by the Beer-Lambert law [77]

$$I(\lambda) = I_0(\lambda) \exp\left(-\mu(\lambda) L\right). \tag{12}$$

The intensity spectra $I(\lambda)$ and $I_0(\lambda)$ are conventionally measured using a spectrometer. A light source is typically chosen such that characteristic variations between $I(\lambda)$ and $I_0(\lambda)$ happen within its spectrum. As the diagnostic name implies, a light source with a spectrum spanning from UV to visible wavelengths is often chosen. Solving Equation 12 for $\mu(\lambda)$ yields

$$\mu(\lambda) = -\frac{\ln\left(I(\lambda)/I_0(\lambda)\right)}{L} \tag{13}$$

The extinction of a gas mixture containing dust with a certain size distribution can be represented as a linear combination for the sizes r with their respective extinction cross-sections $\sigma_r(\lambda)$ and densities $n(r)$,

$$\mu(\lambda) = \sum_{r=0}^{\infty} \sigma_r(\lambda) n(r). \tag{14}$$

From a reference spectrum $I_0(\lambda)$ and a known beam path length L, one can then compare determine the size distribution by combining Equation 14 and Equation 13 such that

$$\sum_{r=0}^{\infty} \sigma_r(\lambda) n(r) = -\frac{\ln\left(I(\lambda)/I_0(\lambda)\right)}{L}. \tag{15}$$

The extinction spectra $\sigma_r(\lambda)$ can be simulated if the refractive index of the particles is known. The average size distribution $n(r)$ over the beam path can then be determined using a fit to minimize squared residuals between the left-hand and right-hand side of Equation 15.

Extinction simulations

As discussed in subsection 2.2, it is well known that particle formation in an HMDSO plasma can be either of monomer-like composition having a high carbon content, or of interlinked SiO_2 structure. The interaction of particles formed from HMDSO with light depends heavily on the chemical and structural composition, which in turn depend heavily on parameters such as plasma power density [78–84]. The (complex) refractive index data used for this work is taken from Saloum *et al.* [81, 82], as they have shown the influence of plasma power and oxygen admixture on the refractive index in the most detail. It must be noted that it is unknown how the potential changes in chemical composition and morphology between low pressure literature translates to the atmospheric pressure work under study here. Recommendations will be made in section 7 as to the best way to cover this potential liability.

The wavelength range of the spectrometer (175 to 1325 nm in steps of 0.56 nm) is taken as the spectral range of the extinction simulation. A particle radius range of 25 to 500 nm was chosen. Smaller particles attenuate

too little light to be able to detect them, and larger particles were not observed in the experiments for this work. Software developed by Schäfer [85] was used to calculate the extinction spectra for each particle radius [76]. Examples of extinction spectra are displayed in Figure 3.1.

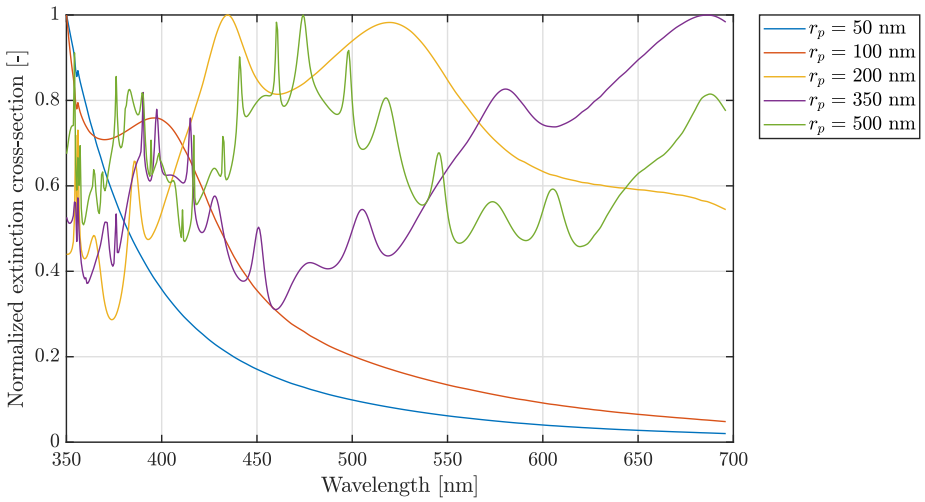

Figure 3.1: *Example (normalized) extinction spectra for various particle sizes.*

Fit procedure

Solving Equation 15 for $n(r)$ in order to minimize the sum of squared residuals comes down to solving a linear non-negative least squares (NNLS) problem

$$Ax = b, \tag{16}$$

where A are the extinction cross-section spectra for sizes r, x are the non-negative size coefficients $n(r)$, and b is the measured extinction spectrum [86]. A Monte-Carlo fit scheme has been used in literature to invert the extinction problem [87, 88]. In this work, we opted for a specifically designed NNLS solver [89, p. 161].

To account for fit tolerances and step sizes, the extinction spectra and measured spectra are normalized to their respective maxima before the fit procedure. After the fitting procedure, the found coefficients $n(r)$ are converted back accordingly.

The measured attenuation spectrum $\mu(\lambda)$ is weighted to account for the influence of instrumental errors. The weights $w(\lambda)$ are taken equal to

$$w(\lambda) \propto \frac{1}{\Delta\mu(\lambda)}, \tag{17}$$

where $\Delta\mu(\lambda)$ is the standard deviation of a measurement in $\mu(\lambda)$. Using Equation 13 it can be deduced that $\Delta\mu(\lambda)$ is dependent on the measurement errors $\Delta I(\lambda)$ and $\Delta I_0(\lambda)$ as

$$\begin{aligned} \Delta\mu(\lambda) &= \left|\frac{\mathrm{d}\mu(\lambda)}{\mathrm{d}I(\lambda)}\right|\Delta I(\lambda) + \left|\frac{\mathrm{d}\mu(\lambda)}{\mathrm{d}I_0(\lambda)}\right|\Delta I_0(\lambda) \\ &= \frac{\Delta I_0(\lambda)}{I_0(\lambda)L} + \frac{\Delta I(\lambda)}{I(\lambda)L}. \end{aligned} \tag{18}$$

The measurement errors are assumed equal and constant throughout the measured spectrum, such that the weights $w(\lambda)$ can be taken

$$w(\lambda) = \frac{1}{1/I_0(\lambda) + 1/I(\lambda)} \tag{19}$$

to satisfy Equation 17, which converges towards $w(\lambda) \propto I(\lambda)$ for low extinction.

Example

An example of the fit procedure executed on a measurement at standard experiment parameters is displayed in Figure 3.2. The corresponding size distribution is displayed in Figure 3.3.

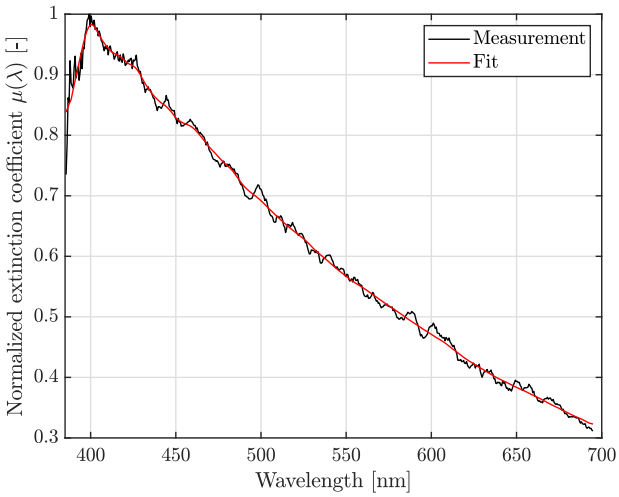

Figure 3.2: *Example normalized measurement of an extinction spectrum (black) and NNLS fit (red). Taken under default experiment parameters.*

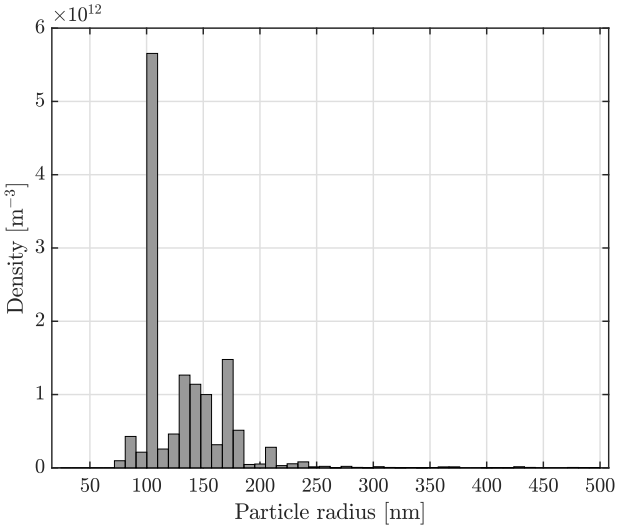

Figure 3.3: *Example binned particle size distribution corresponding to the extinction inversion in Figure 3.2.*

The fit corresponds to an R-squared value of $R^2 = 0.9998$ with respect to the raw signal.

3.2 Electrical probe

As discussed in section 2, the plasma in this work is generated by externally applying an electric field that oscillates with an RF frequency (13.56 MHz). Free electrons respond to this electric field, start following its direction and in their course collide with each other, ions, neutrals and reactor walls. The behaviour of a component (such as a volume filled with plasma) in response to an electric field can be quantified by means of the complex impedance Z. It can be determined as

$$Z = \frac{V}{I} \tag{20}$$

by measuring the voltage V over the component, and the current I flowing through the component. An equally interesting parameter for plasma physicists is the deposited power P, which is defined as

$$P = V \cdot I. \tag{21}$$

To make matters more difficult, the voltage and current oscillate with a period of 73 ns. To accurately measure the voltage, current and power, one has to make measurements that are much faster than the rate of change. Additionally, the measurement has to occur as close to the plasma as possible, because any other components between the plasma and the measuring device have an impedance as well. Beijer *et al.* have developed such device specifically for the setup used in this work [90].

The measurements performed by the multiplying probe are read by an oscilloscope. Voltage and current measurements were found to match sinusoids well, which is not always the case [91]. As a result, the system is fully described by the amplitudes of the P, I, V waveforms. The amplitude $\hat{y}$ of a sinusoidal signal $y \in \{P, I, V\}$ was determined by calculating the root mean square (RMS). To be able to distinguish time-dependence within a voltage pulse, a moving RMS was used,

$$y_{RMS}(i_t) = \sqrt{\frac{1}{2N} \sum_{i=i_t-N}^{i_t+N} y_i^2}. \tag{22}$$

It was found that $N = 10$ yielded enough datapoints to accurately determine the RMS while having good time-resolution. The signal y_i is composed of random noise n_i in addition to the physical signal x_i. Using uncorrelated signal and noise $\langle x_i n_i \rangle = 0$, it is found that

$$x_{RMS}(i_t) = \sqrt{y_{RMS}(i_t)^2 - n_{RMS}^2} \tag{23}$$

where n_{RMS} is determined using a measurement of 0 externally applied voltage.

The amplitude of the physical signal x is found by

$$\hat{x} = 2\sqrt{2} \cdot x_{RMS}. \tag{24}$$

3.3 Scanning Electron Microscopy

As an ex-situ diagnostic technique, Scanning Electron Microscopy (SEM) was used for size determination. In SEM measurements, electrons are directed onto a sample surface. The source electrons either are either backscattered from the surface or free an electron from the sample by secondary electron emission. They can then be viewed using a detector with spatial resolution.

An increased local intensity on the detector image is related to a higher atomic number Z.

Energy Dispersive X-ray Spectroscopy

When electrons are emitted from the sample due to secondary electron emission upon being hit with incident electrons, a vacant orbital is created. The atom is now in an unstable excited state, as there are electrons in higher-energy orbitals (with the exception of the hydrogen atom). The decay of one such electron towards the vacancy emits a photon in order to preserve energy. The energy of the photon is characteristic for the difference in orbital energies, and is therefore a finger print of the atom. The X-ray spectrum generated by these line-emissions can therefore be used to determine the element composition of the sample surface.

4 Experimental setup

This section will describe the experimental setup used in this work. A schematic of the plasma jet and some peripherals is shown in Figure 4.1. It is identical to that used for the works of Platier *et al.* [92] and Staps [93]. The plasma reactor consists of (in order of radial distance) a tungsten needle electrode connected to an RF amplifier, a discharge gap of 0.5 mm, a quartz tube, and a grounded copper electrode. The discharge volume is 45 mm in axial length, measured until the end of the tungsten needle.

A more in-depth description of the experimental setup is estimated to be not relevant for the work discussed in this thesis, but can be found in published work [93].

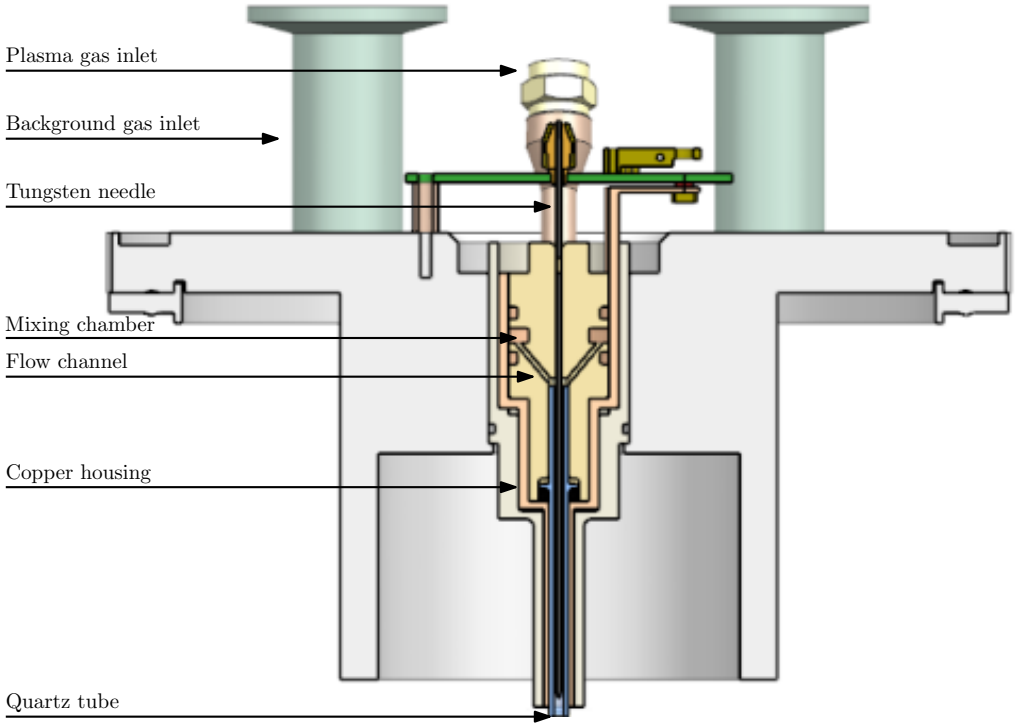

Figure 4.1: *Schematic of the plasma jet setup used for this work. Adapted from Staps [93] with permission.*

The plasma jet flange shown in Figure 4.1 is mounted on a vacuum vessel as shown in Figure 4.2. This vessel is isolated from the surrounding atmosphere to prevent the produced fine dust from entering the laboratory air. Quartz windows are on each side of the vessel to allow for optical diagnostics.

4.1 Electrical setup

An RF signal generator of 13.56 MHz is connected to an RF amplifier. The amplified signal is connected to the needle in the jet, while the copper tube is connected to the electrical ground. Without a plasma, the (radial) gap between the needle and copper tube behaves as a capacitor. With the plasma present it behaves as a (nonlinear) complex impedance. A tunable inductor is added in series with the discharge for impedance matching by compensating for the imaginary (capacitive) part of the impedance, similar to described by Singh *et al.* [94]. If the impedance of the load (i.e. the electrical circuit of the jet setup) is matched to the source (i.e. the RF amplifier), the power transfer of the source to the plasma is optimal.

A power probe was developed by Beijer *et al.* to accurately measure voltage, current and power of the reactor circuit [90]. A capacitive shield is put around the plasma jet in order to fix parasitic capacitance to a constant value, making power probe measurements more reliable.

4.2 Gas flow

A carrier gas of Helium (10^{-5} impurity) is used in this work. The carrier gas is split into three lines. The first line serves as a background flow and is led directly into the vessel as depicted in Figure 4.1. The second line is labelled as a precursor flow. It is first directed through a Mass Flow Controller (MFC), then through a bubbler filled with HMDSO liquid. The last line is connected to the output of the second line and fed into the plasma jet. Of the flow directed through the bubbler, it is assumed that the HMDSO-to-Helium ratio is equal to the vapor pressure relative to the total pressure as per Raoult's law [95]. The vapor pressure of HMDSO is taken as 0.05 atm [96]. The total pressure is assumed to be equal to that of the vessel at 1 atm. The HMDSO content in the precursor gas line is therefore assumed to be approximately 5%.

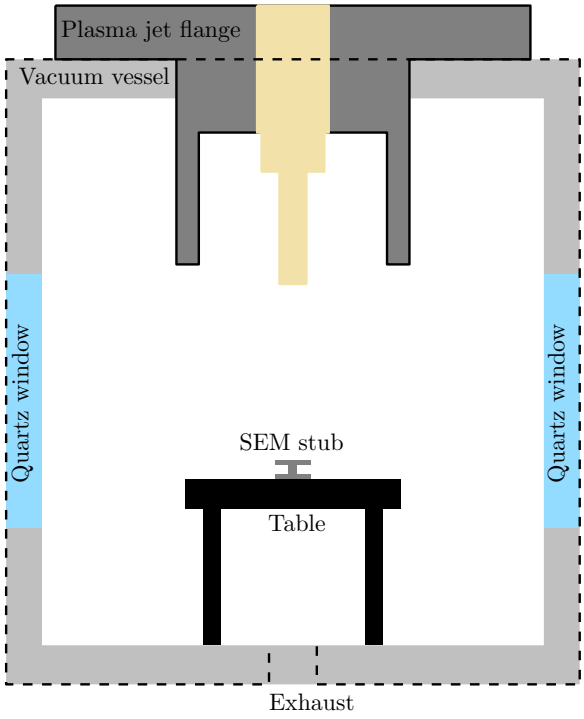

Figure 4.2: *Schematic of the plasma jet flange and vacuum vessel.*

4.3 Diagnostics

The diagnostics from section 3 are implemented into the setup as follows. A light source with a spectrum spanning from near ultraviolet (350 nm) to near infrared (1000 nm) is directed through the jet flow onto a photodetector. To increase the extinction signal, a grounded table was placed just beneath the beam path. The jet flow and the dust cloud in it are spread out over the table such that the extinction is significantly increased. An illustration of this side view is shown in Figure 4.3. It is estimated that at default flow settings, flow resides in the beam path for 2 s. At standard pulse settings, this equates to 20 pulses. The dust density determined from the method detailed above is thus an average of the dust density along the beam path.

As the dust is spread radially outwards over the plate, the density is expected to decrease as $\propto 1/r^2$, assuming circular symmetry. The beam path is estimated to have a length of 10 cm through the dust distribution before the flow is directed out of the beam path. The total beam path is tripled because of the multi-pass technique incorporated in the experimental setup. Using an Abel transformation it is estimated that the actual density, time-averaged, in the plasma reactor is higher than the determined density by a factor of 38 ± 25.

To increase the extinction signal further, a multi-pass technique was used. Mirrors were placed next to the photodetector and the light source. The top view of the configuration is displayed schematically in Figure 4.4. The setup is currently configured as a triple-pass. It is estimated that the beam path through the dust cloud (single-pass) is 10 cm. In addition to the photodetector, a camera has been placed at 90 degree angle with the beam path.

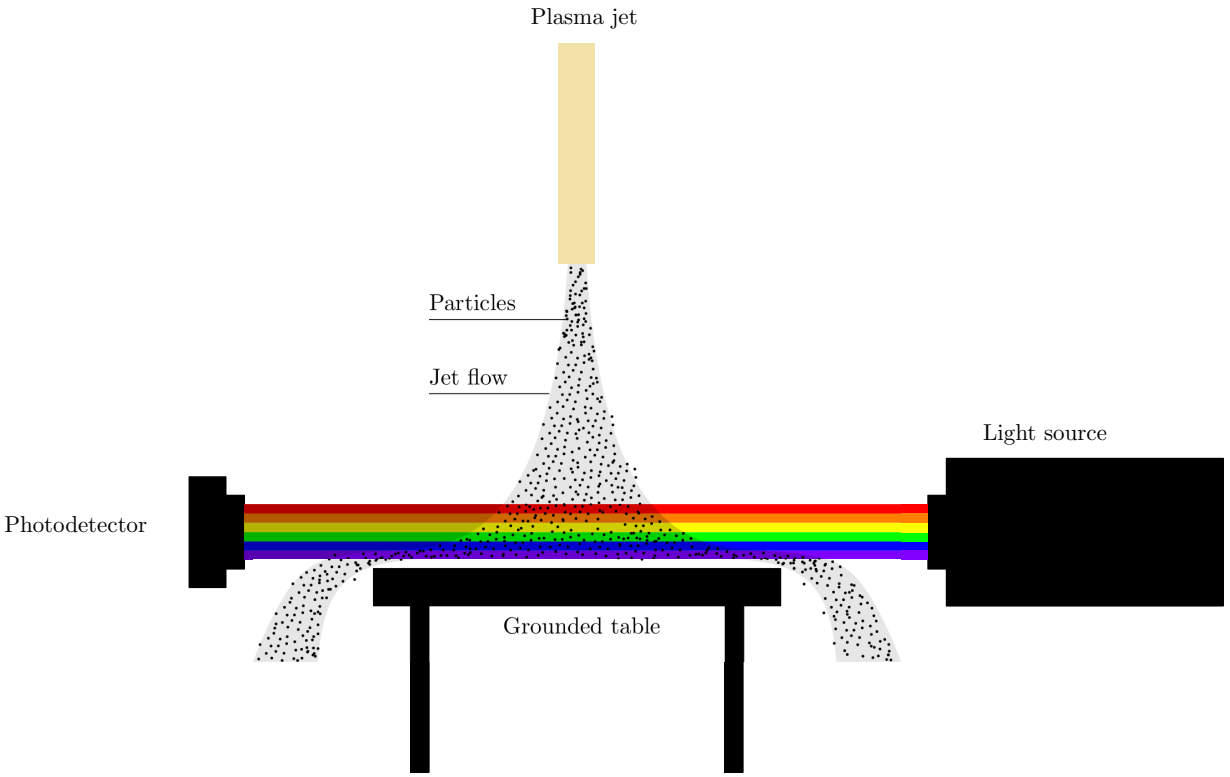

Figure 4.3: *Side view of the UV-Vis diagnostic setup.*

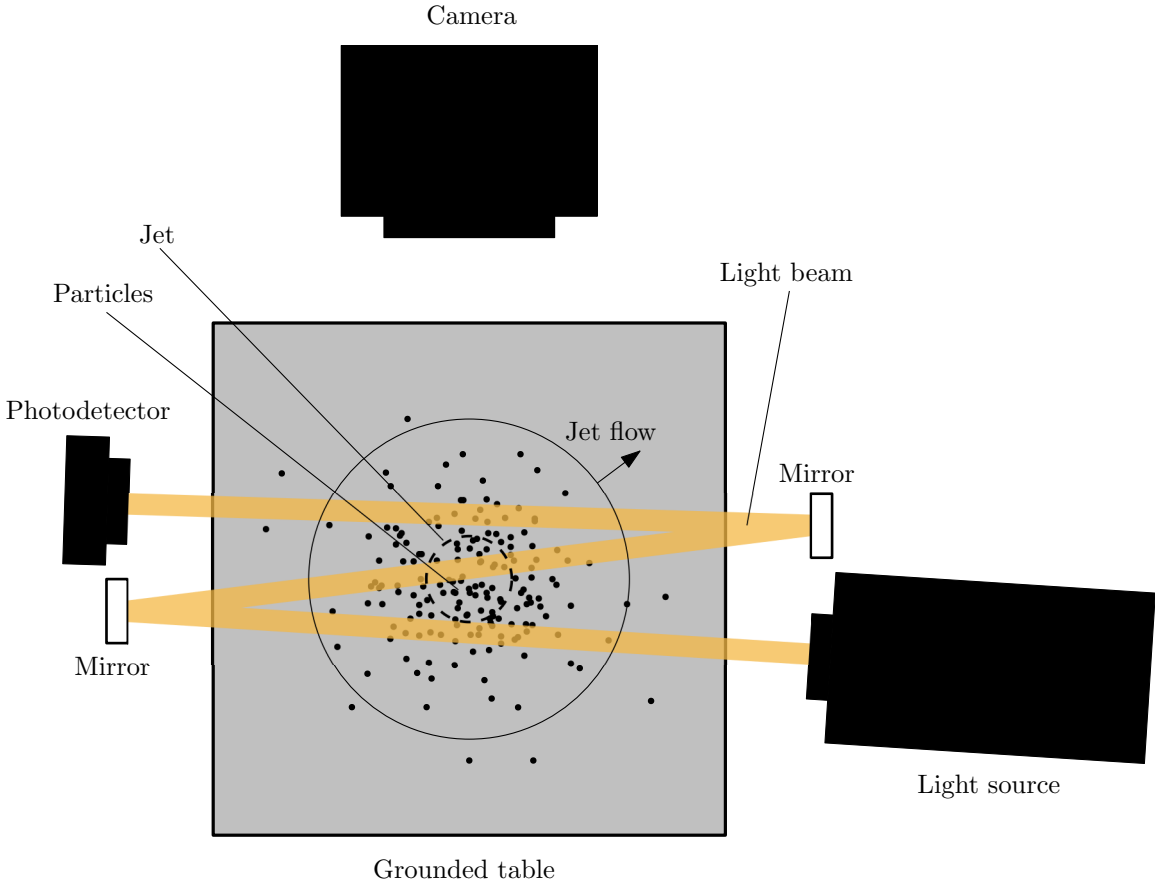

Figure 4.4: *Top view of the UV-Vis diagnostic setup.*

4.4 Experimental parameters

The parameters for the experiments performed in this section are equal to those in Table 4.1 unless stated otherwise.

Parameter	**Default value**	**Relative error**
Power	20 W	2.5×10^{-2}
Duty cycle	20 ms/100 ms	$<10^{-5}$
Pressure	1 atm	$<5 \times 10^{-2}$
Temperature	290 K	$<2 \times 10^{-2}$
Total plasma flow	250 sccm	$<2 \times 10^{-2}$
→ Residence time	22.5 ms	
Plasma carrier gas	Helium	
Oxygen fraction	0	
HMDSO fraction	7×10^{-3}	$\sim 1 \times 10^{-1}$
→ HMDSO flow	1.75 sccm	
Background flow	1000 sccm	$<2 \times 10^{-2}$
Background gas	Helium	

Table 4.1: *Default experiment parameters. Derivative parameters are marked with →.*

5 Results & Discussion

In this section, the influence of control parameters on dust growth will be studied. Aside from the parameter under study, all parameters are kept at the defaults described in Table 4.1.

The experiment duration was 3 minutes for all experiments, with a UV-Vis measurement every 3 seconds. The results displayed in the following sections are calculated on the latest 10 datapoints to allow the system to settle in a steady-state (for e.g. temperature). The size distribution is determined by the UV-Vis method described in subsection 3.1.

5.1 Duty cycle sweep

Description & observations

To gain insight into the temporal characteristics of the particle formation process, a duty cycle sweep was performed. During this experiment, the repetition period was kept constant at 100 ms and the on-time was varied between 2.5 ms and 20 ms. Lower on-times resulted in unacceptably low absorbance-to-noise ratios and unstable plasma pulses, and higher on-times resulted in unacceptably low transmittance-to-noise ratios. For reference, in the parameters employed for this experiment, the residence time of flow inside the plasma volume is estimated at 25 ms. As the residence time is lower than the repetition period, particles in the flow only encounter a single plasma pulse. The on-time of the plasma pulse is therefore equal to the residence time of a particle in plasma. This duty cycle parameter scan is therefore equal to a plasma residence time scan.

The determined particle size for the duty cycle sweep is displayed in Figure 5.1. No significant change in radius between the measurements could be determined. The most probable particle size (i.e. mode) of the fit does not change significantly within the scanned parameter range. The 95% population ranges around the median show a slight upward trend. The particle mode along this parameter scan is 80 to 105 nm.

The determined dust density for the duty cycle sweep is displayed in Figure 5.2. As is expected, the produced dust density diminishes for a duty cycle converging towards zero. The shape of this convergence can yield information on the time dependence of the formation process. In addition, the dust density asymptotically converges to a certain density value for increasing duty cycles.

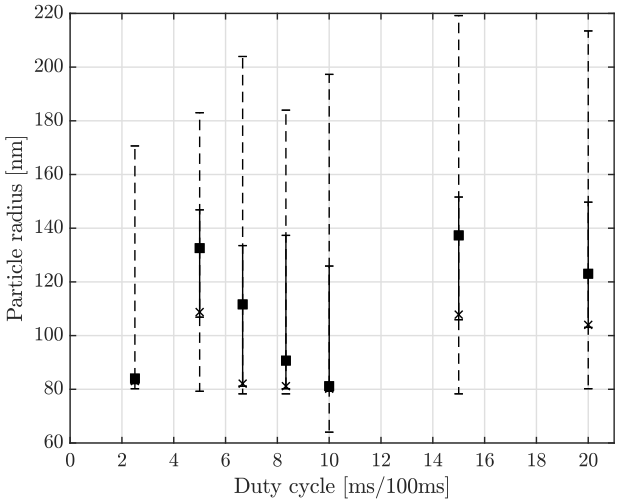

Figure 5.1: *Particle radius information for on-time parameter sweep. Crosses indicate the mode. Squares indicate the median. (Dashed) Error bars indicate the (95%) 50% population centered around the median.*

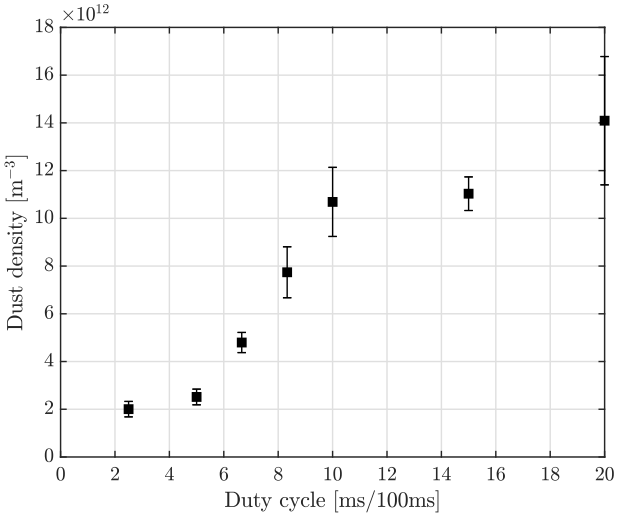

Figure 5.2: *Particle density for on-time parameter sweep. Squares indicate the mean. Error bars indicate 95% confidence interval of the mean.*

Discussion & Conclusions

It is noted that <25 nm particles would not be detected using this method because of their small scattering cross-section. Because no particles 25 to 80 nm in radius are detected for the lowest on-time, it must be concluded that the growth rate $G(r)$ in at least that size range must be very fast compared to the lowest on-time of 2.5 ms. This is in stark contrast from dust growth at low pressure (e.g. 10 Pa), where dust growth to 100 nm takes around a minute [36]. It is suggested that this fast growth rate $G(25\,\text{nm} < r < 80\,\text{nm})$ is the coagulation phase. Additionally, growth rate $G(80\,\text{nm} < r < 200\,\text{nm})$ must be low, because no particles above that range were observed. Those two conclusions alone are, to the best knowledge of the author, new for atmospheric pressure complex plasmas.

The slight upward trend in the median, middle 50%, and middle 95% particle sizes could be explained by growth by means of accretion. The physical setup of the diagnostic would have to be improved to verify this effect because the trend is too unclear to draw conclusions at this point.

If the physical setup could be improved (see section 7), the growth rate of particles in an atmospheric plasma could be mapped by extending the on-time sweep performed here to lower ranges.

The trend in dust density will now be considered. As a longer plasma on-time causes more flow to have encountered plasma, it is more relevant to study the dust production rate than the density. Here, the dust production rate is defined as the ratio between dust volume and percentage of flow exposed to plasma. In the extreme case that a pulse is infinitesimally short, the ratio of exposed flow is the ratio between the flow that resided in the plasma volume during the pulse, and the total flow corresponding to one pulse period. This is equivalent to the ratio of the flow residence time T_{res} to the RF pulse repetition period T_{rep}. To take this effect into account, the probability of a part of the flow being exposed to $T_{exposure}$ of plasma is calculated. The cumulative distribution functions are displayed in Figure 5.3. It can be interpreted as what ratio of the total flow has been exposed to plasma for less than $T_{exposure}$ (x-axis).

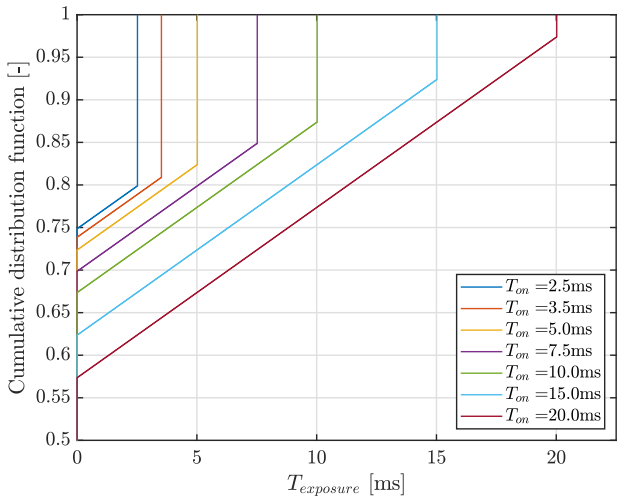

Figure 5.3: *Cumulative distribution function for various plasma on-times.*

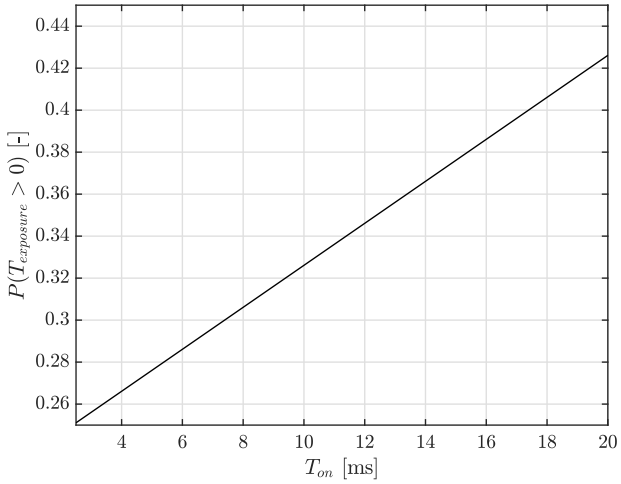

Figure 5.4: *Probability of plasma exposure for various plasma on-times.*

Building on the conclusions earlier in this section, growth must be fast compared to the plasma on-times studied here. Using these simulations it is calculated what percentage of the flow has been exposed to plasma, $P(T_{exposure} > 0)$. This is displayed in Figure 5.4. The exposure ratio linearly goes towards T_{res}/T_{rep}, contrasting the contributions of flow that was already in the discharge volume during its on-time and flow entering the plasma volume during its on-time. Evidently, the former contribution is dominant for low plasma on-times. The dust production rate R is now formally defined as $R \propto V/P(T_{exposure} > 0)$.

The dust volume, defined as the condensed volume of particulate matter

$$V \propto \sum_r \frac{4}{3}\pi r^3 n(r), \tag{25}$$

is displayed in Figure 5.5. Note that this value will be displayed in arbitrary units. This graph is a measure of the conversion from HMDSO in gas-phase to solid particles. The production rate is displayed in Figure 5.6.

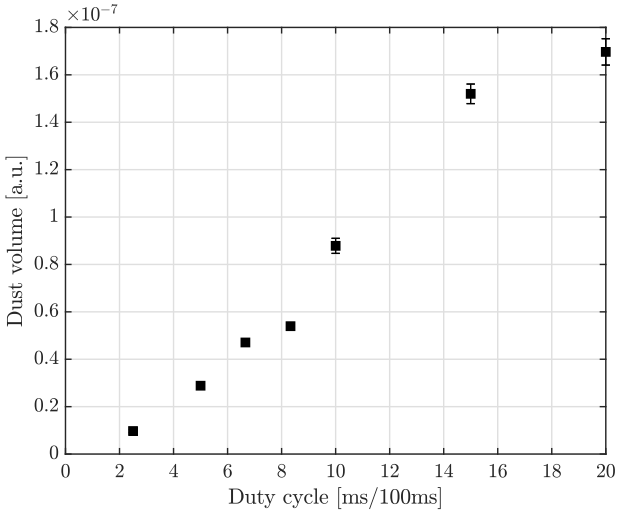

Figure 5.5: *Particulate volume for on-time parameter sweep. Squares indicate mean of performed measurements. Error bars indicate 95% confidence interval of the mean.*

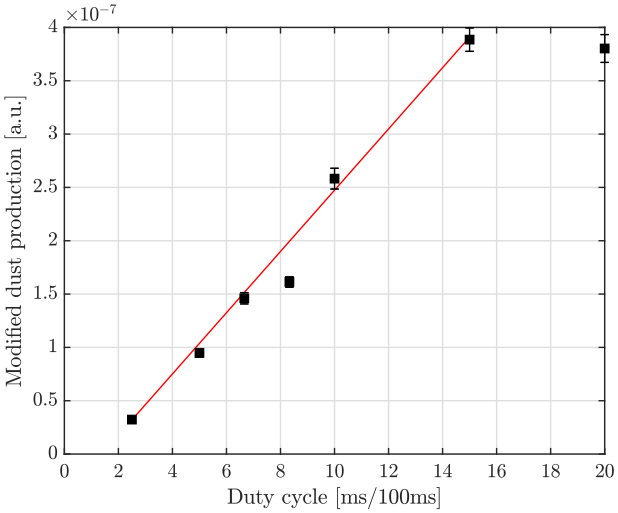

Figure 5.6: *Dust production rate for on-time parameter sweep. Squares indicate mean of performed measurements. Error bars indicate 95% confidence interval of the mean. Red line is added to guide the eye.*

Firstly, it is observed that the production rate increases linearly with plasma on-time, except for the 20 ms data point. From the size distribution in Figure 5.1 and density data in Figure 5.2, it can be concluded that the change in production rate is dominantly caused by a higher density of particles as opposed to larger particles. Previously, it was concluded that the particles observed here are after the coagulation phase. This leads to the hypothesis that, for a lower plasma on-time, there are fewer nuclei to coagulate into observable particles.

The 'slow nucleation phase' hypothesis is in parallel with knowledge of dust growth at low pressure [34]. Based on the equal production rate of 15 ms and 20 ms on-times, it is concluded that HMDSO depletion into particle nuclei happens on a 15 ms timescale.

In conclusion:

- The process of particle growth from 25 nm (diagnostic sensitivity) to 80 nm (the lowest observed size) in radius must be significantly faster than 2.5 ms.
- To account for a decreased production at lower duty cycles, there must be a slow process before the 25 nm radius. It is suggested that this is the conversion of HMDSO into particle nuclei. The timescale of HMDSO depletion is determined to be 15 ms.
- The duty cycle parameter also influences the effective power deposition of the plasma onto the reactor, and thereby changes the reactor temperature. It is important to take this into account when designing a dust production device.

5.2 Power sweep

Description & observations

A plasma power sweep between was performed to investigate the influence of the power parameter on dust growth. The maximum achievable power with the instruments in this setup was ∼24 W. The minimum achievable power for which voltage pulses ignited the plasma with sufficient reproducibility was ∼11 W.

The particle size is displayed in Figure 5.7. It can be seen that the observed particle sizes do not change significantly, with the exception of 11.5 W, where the median, mode, middle 50% and middle 95% particle sizes are all lower than in the rest of the power scan.

The total detected particle density is displayed in Figure 5.8. It can be seen that the total density of produced dust significantly changes in the power range explored for this experiment.

The dust production rate is shown in Figure 5.9. It appears that conversion from HMDSO in gas-phase to solid particles is most efficient for the 16 to 22 W range, within the parameters used for this experiment.

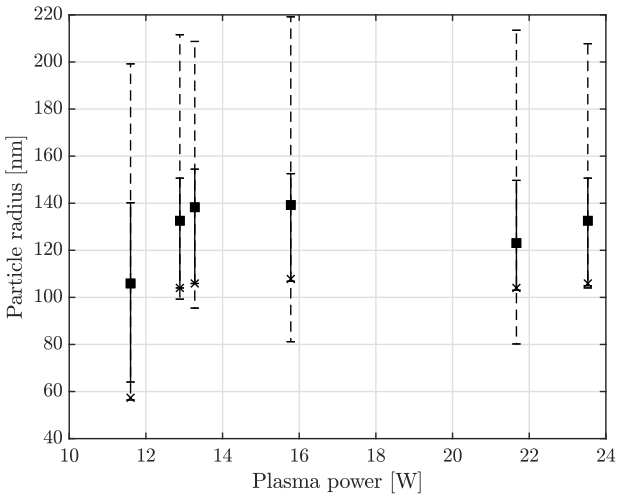

Figure 5.7: *Particle radius information for plasma power parameter sweep. Crosses indicate the mode. Squares indicate the median. (Dashed) Error bars indicate the (95%) 50% population centered around the median.*

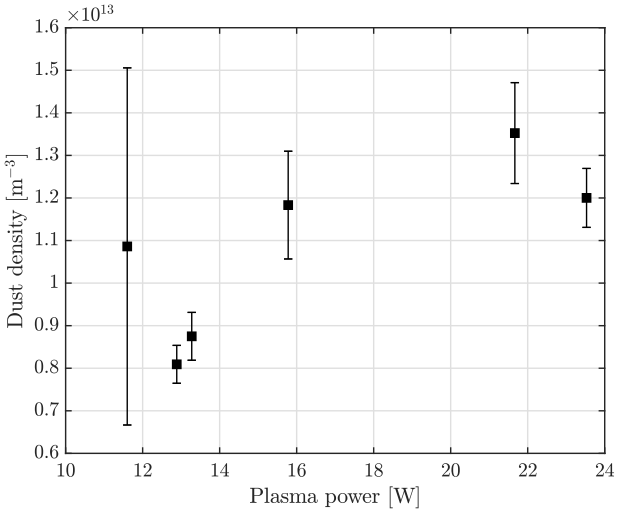

Figure 5.8: *Particle density for power parameter sweep. Squares indicate the mean. Error bars indicate 95% confidence interval of the mean.*

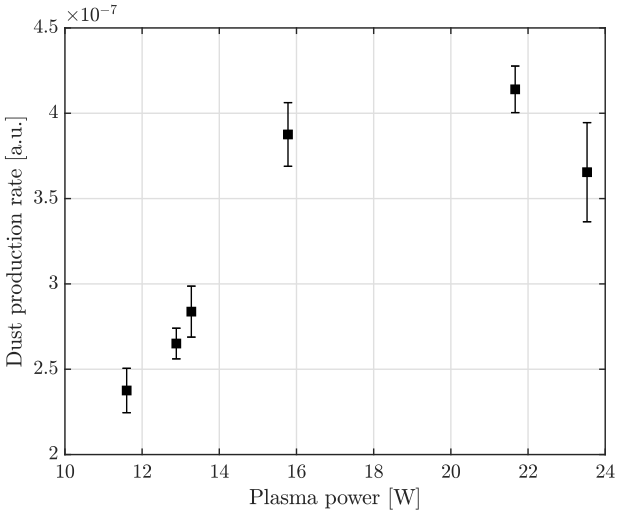

Figure 5.9: *Mean particulate volume of matter for plasma power parameter sweep. Error bars indicate 95% confidence interval of the mean.*

Discussion & Conclusions

Several conclusions can be drawn from this experiment. As the dust production shows a clear trend, it is apparent that there is still some precursor left after the gas leaves the plasma area, i.e. the HMDSO was not depleted. This is an interesting observation when combined with the fact that the radius mode did not vary significantly.

To be able to draw conclusions from this data, it is important to understand the influence of the parameter under study. The power parameter influences a number of environmental parameters inside the plasma reactor.

Firstly, increasing power absorption by the reactor increases power deposition in the gas and reactor walls in the form of heat. As discussed in subsection 2.2, temperature has a significant impact on dust production. Its first influence is flow-related. An increase in temperature will lead to a higher gas flow speed in order to maintain pressure (causing a shorter plasma residence time) while lowering the number density (which has an unknown effect). Its second influence is directly on HMDSO(-fragment) reaction rates [32, 43, 97] (subsection 5.3).

Secondly, the electron density strongly increases with power. From measurements performed with a multiplying probe [90] on pure Helium plasma performed with this setup, electron densities between 1×10^{20} and 1×10^{21} were found in the 5 to 25 W power range, which can be used as a rough estimation for the electron density change in an Helium-HMDSO plasma. Higher electron density causes reactions with electrons (e.g. dissociation, radical production, ionization) to take place proportionally more frequently.

The constant particle size leads to the conclusion that the increased production of ions and radicals by a higher electron density is balanced by a higher particle density. This is confirmed by the increasing flank (21.5 W) of the plasma power scan. The decrease in dust density and production above 21.5 W is suggested to be caused by heating effects and will be further discussed in subsection 5.3. The constant particle size distribution throughout the power range remains difficult to explain. It can be concluded that the size distribution is not influenced by the density of nuclei with the exception of lower powers.

- Reasoning from elimination and referencing the literature presented in subsection 2.2 it is hypothesized that an increasing electron density has a stimulating effect on nuclei formation, whereas a higher gas temperature decreases nuclei formation. The hypothesis on the influence of temperature on the production of particles will be further tested in subsection 5.3.
- The power parameter therefore inconveniently influences two counteracting physical parameters. It is suggested to take this into account when designing a dust producing device, and that the repetition period can be used to tune the time-averaged power thereby preventing temperature effects.

5.3 Heating power sweep

It is expected that gas temperature has a significant influence on dust growth, both due to literature discussed in subsection 2.2 and the unexpected decrease in production for high plasma powers. The plasma is the most direct way to deposit heat onto the plasma reactor. Plasma on-times larger than the flow residence time (25 ms) do not contribute to longer growth times for particles, but do contribute to a larger effective heating power $P_{eff} = P_{plasma}\frac{T_{on}}{T_{rep}}$ on the reactor. The on-time is therefore scanned from 25 to 100 ms. On-times smaller than 25 ms were taken from subsection 5.1 and included for completeness.

The particle radius is shown in Figure 5.10 and shows a wavy trend: increasing particle radii for P_{eff}<5 W, decreasing for 4 to 6 W, and increasing for >9 W.

The particle densities (Figure 5.11) and production rates (Figure 5.12) show similar trends.

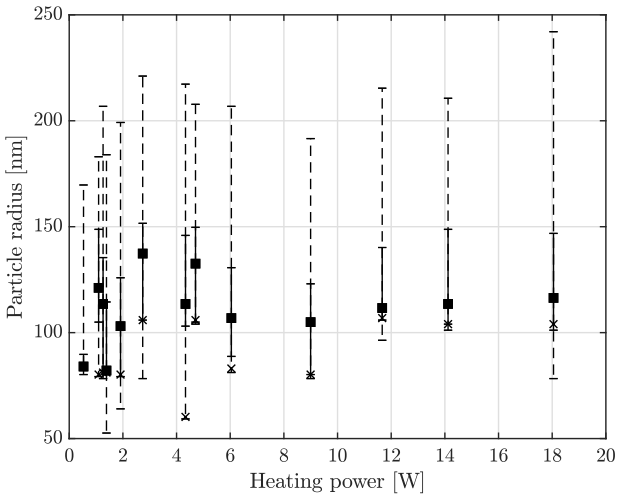

Figure 5.10: *Particle radius information for plasma power parameter sweep. Crosses indicate the mode. Squares indicate the median. (Dashed) Error bars indicate the (95%) 50% population centered around the median.*

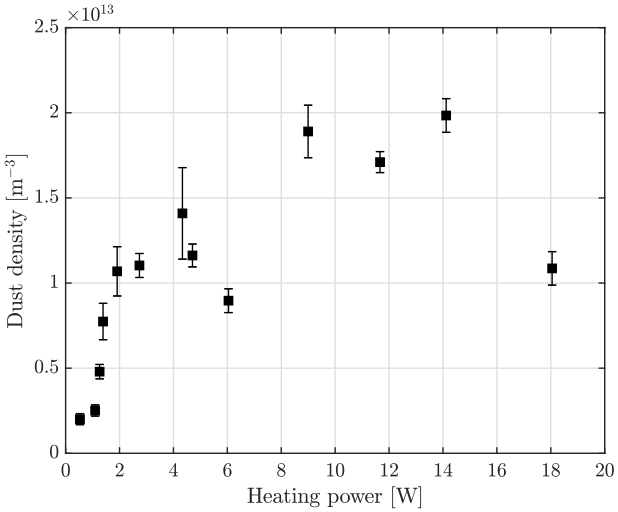

Figure 5.11: *Particle density for power parameter sweep. Squares indicate the mean. Error bars indicate 95% confidence interval of the mean.*

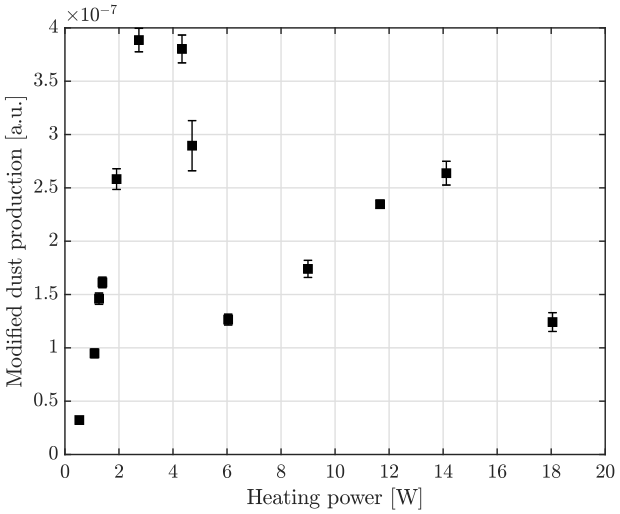

Figure 5.12: *Mean particulate volume of matter for power parameter sweep. Error bars indicate 95% confidence interval of the mean.*

Discussion & Conclusions

It is known that gas temperature significantly effects clustering and coagulation of small particles, resulting in different particle sizes for different gas temperatures [98]. Temperature also was shown to have an effect on the consumption rate of precursor gas in low pressure conditions [34]. The aforementioned effects of temperature on dissociation rate, polymerization reaction rate, residence time and number density also play an unknown role.

This parameter is therefore left purely descriptive: indeed, temperature has a large influence on growth rate. With temperature measurements of the gas and reactor, more information on the influence of temperature can be uncovered.

- The temperature parameter inconveniently also influences flow speed and number density. Decreasing the flow speed setting proportional to the temperature increase can correct for the changing residence time caused by a temperature increase. The decreased number density influences the growth rate in an unknown way, and further research is needed to study its effect more in-depth.

5.4 HMDSO flow

Description & observations

Next, the HMDSO flow was varied while the total plasma flow was kept constant. The particle radius is displayed in Figure 5.13. The median and the range of radii that contains 50% of the population appear to not change significantly under influence of the HMDSO ratio. The particle radius mode is lower for low HMDSO ratios but shows no clear trend.

The dust density (Figure 5.14) significantly decreases for increased HMDSO flow. The increased density at 1.1 sccm appears to be accompanied by the smaller particle radius detected at that HMDSO flow.

During these measurements, it was found that the power decreased significantly for increased HMDSO flows. Other experiments did not show this behavior. For this reason, the plasma power measurements are included here and shown in Figure 5.16.

Lastly, the dust production rate is shown in Figure 5.15 so that it can be compared to Figure 5.9.

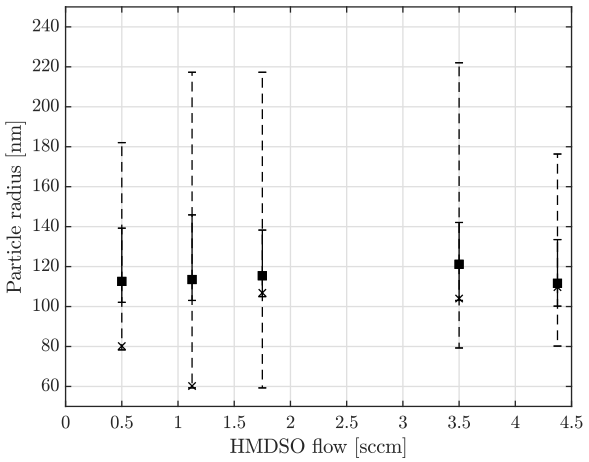

Figure 5.13: *Particle radius information for HMDSO flow parameter sweep. Crosses indicate the mode. Squares indicate the median. (Dashed) Error bars indicate the (95%) 50% population centered around the median.*

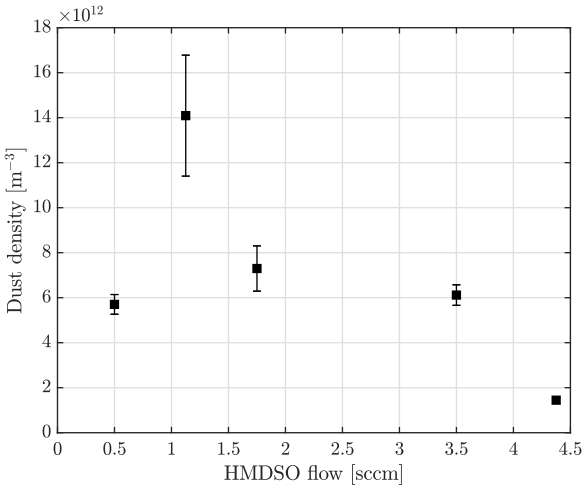

Figure 5.14: *Particle density for HMDSO flow parameter sweep. Squares indicate the mean. Error bars indicate 95% confidence interval of the mean.*

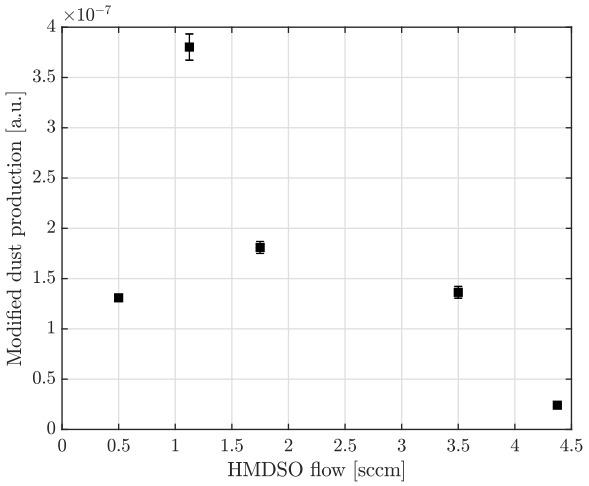

Figure 5.15: *Mean particle density for HMDSO flow parameter sweep. Squares indicate mean of performed measurements. Error bars indicate 95% confidence interval of the mean.*

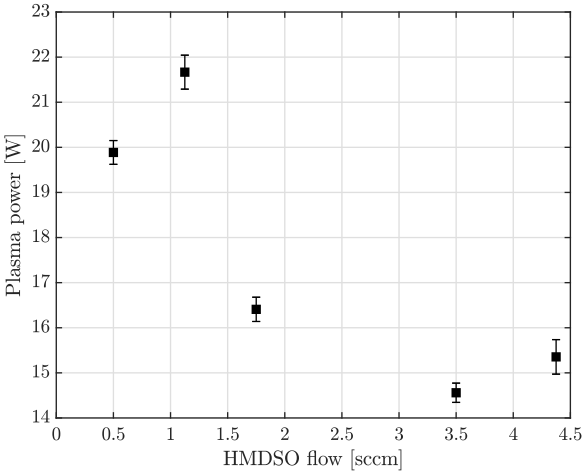

Figure 5.16: *Plasma power for the HMDSO flow parameter sweep. Error bars indicate 95% confidence interval of the mean.*

Discussion & Conclusions

Because of the inconsistency of power in this parameter sweep relative to the other measurements, it will be discussed here first. Matching was kept constant during this experiment, meaning the inductance of the matching coil was not changed. It can be concluded that the impedance of the plasma did change under influence of the HMDSO ratio so that the power absorbed by the plasma declined from its optimally matched value. The plasma impedance consists of a real component related to resistivity (correlated to electron scattering/absorption cross-section) and capacity (caused by a plasma sheath). It is suggested that the presence of HMDSO as the only molecular species increases the gas temperature due to more efficient energy transfer from electrons to ro-vibrational energy levels. Furthermore, molecule dissociation leads to an increased number density which tries to equilibrate by increasing the flow velocity (and thereby decreasing the residence time). Lastly, it is likely that the scattering cross-sections of HMDSO fragments are larger than that of Helium. All these components affect the impedance of the plasma, leading to mismatching and a lower power absorption by the plasma. Effects of molecular species in a complex atmospheric pressure plasma influencing the electron density are covered in literature as well [44].

It is difficult to study the effects of HMDSO flow with changes of plasma power interfering. What is expected is that for high HMDSO flows, the same behavior as for low plasma powers is seen. Constant plasma power with increasing HMDSO flow decreases the deposited power per monomer and is therefore expected to decrease fragmentation, which influences the growth rate of particles.

- HMDSO admixture causes different electron characteristics (e.g. density, energy) that can affect plasma power absorption and dust growth processes.
- A higher HMDSO admixture will cause less deposited power per monomer. This is hypothesized to decrease particle growth.

5.5 Validation

The development of any new diagnostic calls for the validation using an independent diagnostic. In the case of dust production, the most obvious diagnostic to determine dust size distribution is Scanning Electron Microscopy (SEM).

Description & observations

Aluminum SEM stubs were prepared by placing them on the grounded table 5 cm below the plasma jet outlet and exposing them to 10 minutes of plasma flow under default experiment parameters. Micrographs at different scales of this stub exposed to dust are shown in Figures 5.17b to 5.17d. A reference micrograph is made of a stub that was not exposed to dust is shown in Figure 5.17a.

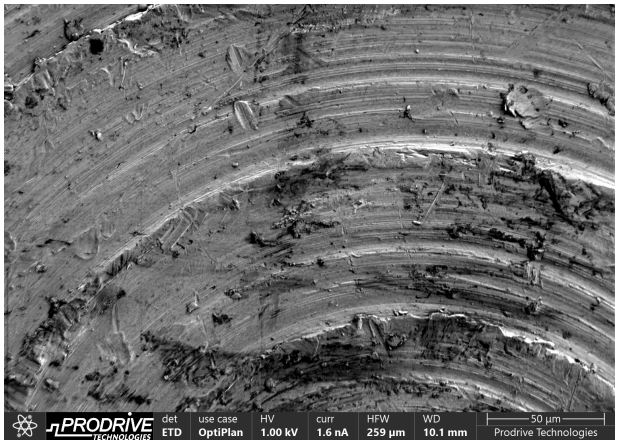

(a) 50 µm - *Unexposed stub for reference.*

(b) 50 µm - *Exposed stub.*

(c) 20 µm - *Exposed stub.*

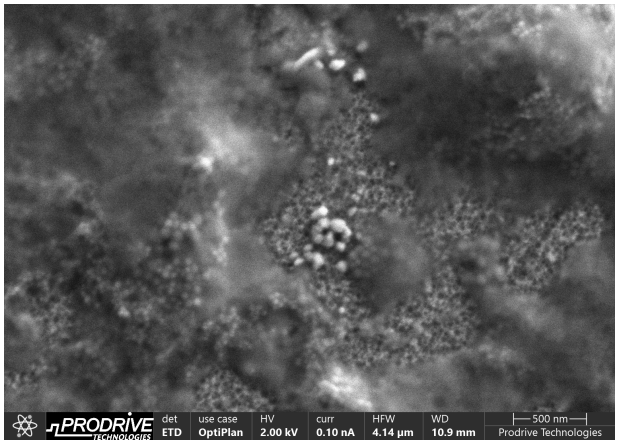

(d) 0.5 µm - *Exposed stub.*

Figure 5.17: *Micrographs at different scales, taken of SEM stubs exposed to dust flow under default experiment conditions.*

Compared to the reference images, the difference is the presence of some kind of amorphous structures.

First, it is noted that the coverage of the SEM stub is low when accounting for the calculated dust density of the order of $1 \times 10^{13}\,\mathrm{m}^{-3}$. The SEM stub was placed on the plasma jet axis, which contains an even higher dust density than the average over the beam path. Coverage of the whole electrode in deposited material was expected.

Second, it is noted that the structures spotted on the exposed SEM stub are highly amorphous and not spherical at all. The structures look as if fused or molten onto the metal stub.

Lastly, it is noted that Figure 5.17d is highly atypical for images acquired at that scale. Spherical particles appear present in high numbers, but covered by a translucent layer of other material. Most micrographs at that

scale did not show any spherical particles.

Discussion & Conclusions

The amorphous structures (rather than spherical particles) are highly unexpected for dust-producing plasmas. A typical micrograph of dust produced by a low-pressure plasma is shown in Figure 5.18. Micrographs obtained on this setup in different experimental conditions are shown in Figure 5.19, which also show at least some evidence of clustered spherical particles.

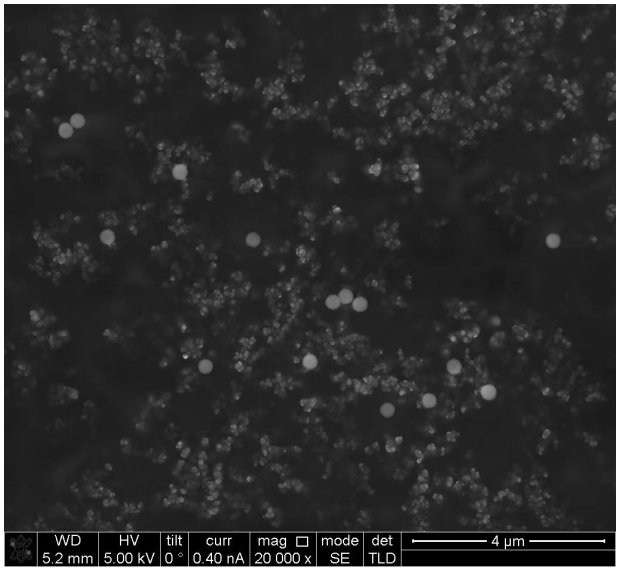

Figure 5.18: *Micrograph of dust produced under low pressure conditions. [99]*

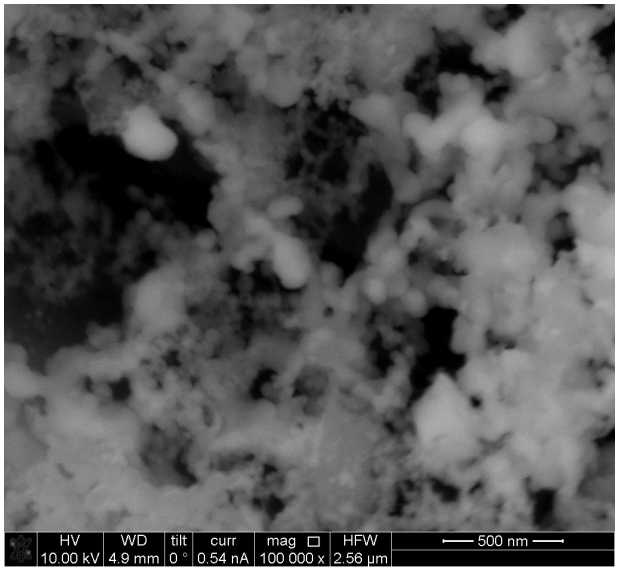

(a) *Micrograph of dust produced under high pressure conditions. Courtesy of T.J.A. Staps.*

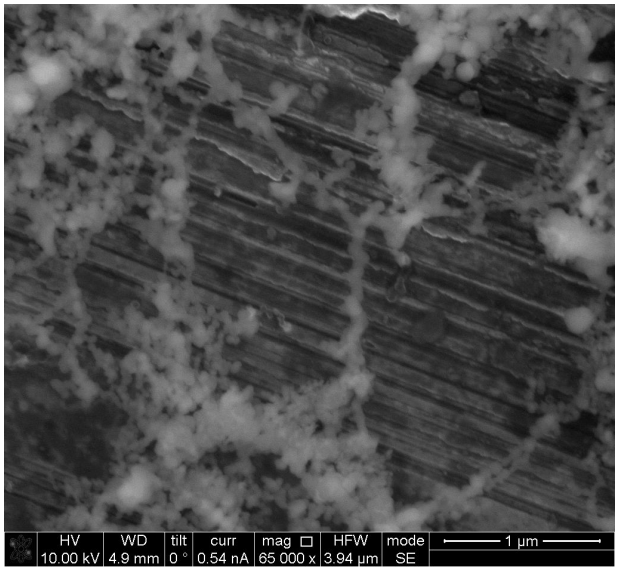

(b) *Micrograph of dust produced under high pressure conditions. Courtesy of T.J.A. Staps.*

Figure 5.19: *Micrograph of dust produced under high pressure conditions.*

There are three categories of reasons for the absence of spherical particles. Firstly, there are no spherical particles. Based on the fact that previous similar research [43, 44], as well as previous experiments on this setup, have produced spherical particles makes this highly unlikely. Secondly, the spherical particles do not come into contact with the SEM stub. This seems plausible, as a thick ($\sim$1 cm) flow boundary layer is formed

above the SEM stub, which might prevent particles from dropping onto the SEM stub. The SEM stub was metallic and grounded, so no charging effects should be at play here. Lastly, particles do not stick to the surface and get blown away by the flow. This also seems plausible. Adhesive carbon tapes for SEM stubs exist, but they were not opted for because the intention was to do EDX analysis on the particles.

One possible explanation of the presence of these structures would be some kind of inhomogeneous film deposition resulting from radicals present in the gas flow.

Particles within the atypical micrograph of Figure 5.17d would be too small to be of significant influence to the extinction measurements in this work. On the basis of all these arguments, it is deemed highly unlikely that the dust sample studied here is representative of the dust population produced by the plasma. Research on atmospheric pressure plasmas is often accompanied by electrostatic precipitator collection of dust particles rather than direct deposition onto a SEM stub [43, 44]. It is concluded that this is the only way of having a good validation of the methods described in this work.

6 Conclusion

In this work, fine dust growth in atmospheric pressure plasmas was studied. Specifically, research has been done to study how the growth process is influenced by various environmental parameters. To that end, a UV-Vis extinction spectroscopy diagnostic has been developed to study the particle size distributions produced by an atmospheric pressure plasma jet.

Under default conditions, the most common particle radius (mode) detected in the dust cloud was found to be 104 nm. 50% (95%) of the observed particles was found to have a radius in the 100 to 150 nm (80 to 210 nm) range. The dust density was found to be $1.4 \times 10^{13}\,\mathrm{m}^{-3}$.

The pulse on-time parameter was found to have no significant impact on the produced particle radius. This strongly indicates that the growth process up until the observed particle sizes is much faster than the lowest on-time that could be studied here, i.e. 2.5 ms. This conclusion could thus far never be made in literature on atmospheric pressure. Pulse on-time was found to have a significant impact on the produced dust density, suggesting that there is a slow initial phase (e.g. particle nucleation) that limits production. A simple growth model was suggested to show that the slow process happens on a 15 ms timescale. Next, it was concluded that growth must be slow in the observed particle size range because no particles with a larger size were detected. It is hypothesized that this is the accretion process, which is known to be slow in low-pressure complex plasmas.

The plasma power parameter was also found to have no significant impact on the produced particle radius. It is suggested that is caused by the conflicting effects that a higher electron density has. It both causes a higher threshold for particle coagulation and higher nucleus growth due to radical production. This is in line with suggestions from literature. Plasma power is found to have a significant influence on the produced dust density. This is linked to the higher production of radicals.

Heating power was found to significantly impact particle size distributions and densities. A clear, but inexplicable trend, was observed in the dust production rate. There are many possible processes that are influenced by gas temperature, so no conclusions could be drawn on the cause of the trend.

The ratio of HMDSO admixture did not largely influence the particle sizes. Large HMDSO flows were found to decrease dust production. This is hypothesized to be caused by a lower power deposition per monomer, decreasing radical production.

In conclusion, it is found that the generated particle size distribution is relatively monodisperse and not largely influenced by any of the parameter ranges scanned for this work. For putting this technology to use in UFP sensor and filter research, this is good news: a plasma jet is a viable source of fine dust with high reproducibility. It is expected that even smaller particles are produced for on-times $<$2.5 ms, but those could not be detected using the current setup. Suggestions for adjustments to the setup to measure smaller particles will be made in section 7.

For applications with larger dust, such as PM2.5, the plasma jet is not as immediately usable. Adjustments would have to be made to the setup to try making larger particles. Suggestions will be made in section 8.

7 Outlook & Recommendations

A lot of lessons are learned to take into account when designing a next-generation fine dust-producing plasma jet. Considerations and suggestions will be made in section 8. As for the scientific contributions made in this thesis, the author estimates them as well-grounded but not definitive. In this section, suggestions for future research are made that could support the hypotheses that were developed for this work. Almost by definition, that entails relaxing some of the assumptions.

7.1 UV-Vis extinction spectroscopy

First and foremost, the method should be validated better. The assumption of spherical particles was roughly confirmed using SEM and on the basis of recrystallization [46, 75]. It is suggested to validate the dust size distribution using Scanning Electron Microscopy (SEM) or Transmission Electron Microscopy (TEM) as well. To avoid any kind of filtering of the size distribution when depositing onto the SEM stub or TEM grid, it is suggested to use an electrostatic precipitation technique that has been used in literature to validate dust size distributions with other diagnostic methods successfully [43, 44]. As an additional method of validating the method, experiments on particles with known size and refractive index, suspended in liquid or gas, are suggested.

It is also suggested that the assumption on the refractive index is relaxed, i.e. it is determined specifically for the dust produced using this plasma jet prior to applying the UV-Vis method. This is by far the most uncertain assumption, as it was shown in subsection 2.2 that particle composition is sensitive for growth parameters such as power and oxygen admixture. Various methods are possible, but all of them need an additional measurement. Adjusting the setup such that angle-dependent scattering of laser light can be measured in addition to the visible light extinction measurement enables the determination of the refractive index in-situ [100, 101]. Alternatively and preferably, spectroscopic ellipsometry can be used to determine the refractive index in-situ.

Additionally, it is suggested to use a lamp and spectrometer combination intended for slightly lower wavelengths than the current setup. The lower wavelength limit of the current setup is 380 nm, but particles below 100 nm radius have their most characteristic features (e.g. peaks) and highest extinction in the 300 to 400 nm range. Particles of small sizes have a low extinction signal, so it might be necessary to extend the usage of the multipass technique to cause a beam path of the order of $\frac{1}{\mu(\lambda)}$.

Lastly, it is recommended to add optical elements to the setup such that the UV-Vis light source is a thin parallel beam. In the current setup, the light beam was slightly divergent, leading to a high integration time or high measurement noise. Similarly, it is recommended to upgrade to a higher class spectrometer. Water cooling to reduce thermal noise would prove beneficial.

7.2 Other diagnostics

After the suggestions to improve the current research and diagnostic methods above, suggestions for additional research will be made below. The process of dust growth on atmospheric pressure is still relatively unknown. To support the current hypotheses regarding the duration of the dust growth process, it is necessary to have diagnostic methods with a measurement repetition period that is much smaller than 2.5 ms. This goes hand in hand with adding diagnostic methods that are sensitive to particles with a 0 to 50 nm radius. Suggestions will be made below.

In conjunction with the adjustments made in section 8, it is suggested to make the reactor walls of a transparent material (e.g. quartz) such that the temporal evolution of the dust could be studied more in-depth.

In parallel with the research performed on dust growth at low pressure, it is recommended to study the electron density and electron temperature behavior during the dust growth cycle. At low pressure, the electron density decreases steeply during the coagulation phase, and electron temperature rises throughout [102]. Specifically, Trace Rare Gas Optical Emission Spectroscopy (TRG-OES) is recommended [103].

To better study the initial phases of dust growth, it is recommended to add mass spectroscopy (MS) to the setup. With a pulsed RF jet, it would be possible to study the time evolution of radicals and other neutrals by sweeping the plasma on-time.

7.3 Control

Building on the knowledge of literature in subsection 2.2, growth is a process dominated by radicals and coagulation is a process inhibited by free charge.

While this process is not fully understood after the efforts in this work, some experiments can be devised to take advantage of the distinction between radicals and ions. While the ions are quickly lost after the plasma is turned off, the radicals survive longer than milliseconds [104]. This is evidenced by the very fact that HMDSO plasmas are used for atmospheric pressure thin film deposition in or even outside the spatial afterglow. If radicals can be controlled separately from ions, that yields an additional control opportunity to e.g. make coagulation occur faster. A doubly pulsed RF signal (i.e. the pulse in section 4 is further divided into sub-pulses) can be a tactic to promote growth while explicitly not preventing coagulation. A similar scheme was previously proposed on low pressure [64] to stimulate high-quality thin film deposition, but here we suggest that it can be applied for usage in atmospheric pressure dust growth as well. Similarly, inducing a voltage lowering step mid-pulse can lower the coagulation threshold. These are the kind of control schemes that might be of great benefit to the goal of this work.

8 Concept design of a plasma jet fine dust generator

The interests of Prodrive Technologies for the development of this plasma jet are for usage in research. Using a controllable dust source, one could study the sensitivity of an air quality sensor for different particle sizes. Calibrations can be executed to match signals of the sensors to real concentrations. The efficiency of filters can be studied in depth, e.g. their efficiency for different concentrations or particle sizes. In this section a concept design will be proposed for such a plasma jet. Some system requirements originating from this application are listed in subsection 8.1.

A dust producing plasma jet has a large amount of design parameters that need to be considered. They can be grouped into plasma reactor geometry (subsection 8.2), precursor mixing (subsection 8.3) and gas flow geometry (subsection 8.4). A proposal combining the design parameters will be made in subsection 8.5.

8.1 System requirements

Listed below are some initial requirements for the dust production that can be achieved with a plasma jet. Given the fact that this is a research project, there is no guarantee that the requirements can actually be met using the studied plasma jet, but these requirements give handholds in deciding what to investigate.

Requirement 1. The total particle mass concentration shall be adjustable. The maximum achievable concentration should be $1000\,\mu g\,m^{-3}$ for lifetime testing. The minimum concentration shall be at most $5\,\mu g\,m^{-3}$ for sensitivity testing.

This requirement can be met using the current plasma jet setup and experiment designs.

Requirement 2. The size distribution must be controllable. There is current interest in PM2.5 and future interest in PM0.1, so particle sizes between 50 nm and 2.5 µm should be achievable.

In the experiments performed in this work it was shown that particle sizes in the 120 to 400 nm diameter range are currently produced. It is probable that smaller particles could be made using shorter plasma on-times so that the lower requirement can be met, but they could not be detected using the current diagnostic methods. The upper requirement requires a longer residence time in plasma volume, which has to be taken into account in the concept design of a new jet.

Requirement 3. The deviation in particle size and concentration compared to their setpoints should be $< 1\%$.

Reproducibility of the plasma jet has been experienced to be inconsistent in the experiments performed during this graduation project. It is suspected that electrode wear is the underlying cause, as will be discussed below.

Requirement 4. The operating lifetime of the device shall be at least 1000 hours.

In the plasma jet used in this work, the operating lifetime was severely limited (<20 hours) by dust contamination and film deposition inside the plasma reactor.

8.2 Plasma reactor geometry

The geometry and properties of the electrodes largely determine the characteristics of the plasma. In this section, distinctions in various areas are highlighted. Various reactor designs are displayed in Figure 8.1, which will be discussed further in the text below.

(a) *Picture of the COST jet with ignited plasma. Clearly shown is the co-planar electrode configuration. [105]*

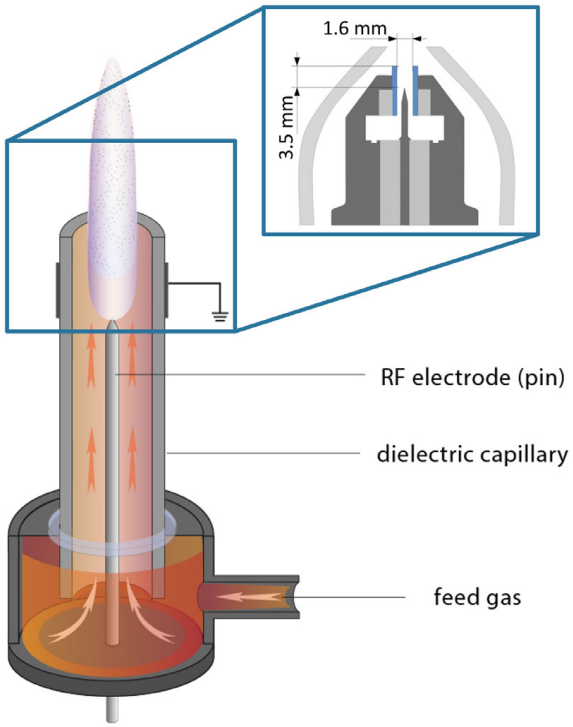

(b) *Schematic of the kINPen plasma jet. Co-axial setup (pin & ring) is clearly shown. [106]*

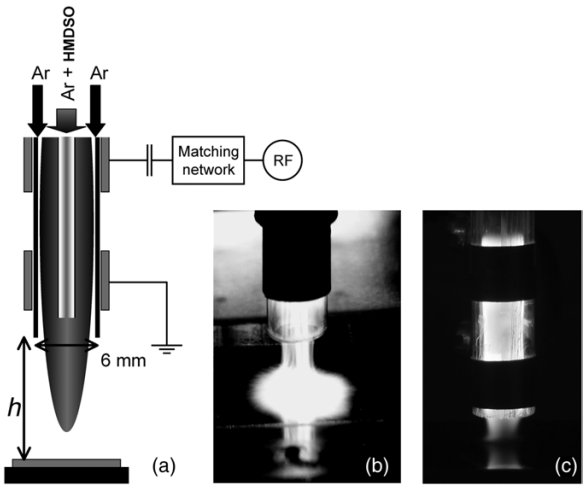

(c) *Schematic of a ring-ring plasma jet setup (a) and two pictures of the jet in operation (b,c). [107]*

Figure 8.1: *Various reactor designs.*

8.2.1 Discharge type

There are various types of discharges that are distinct in their characteristics (e.g. electron temperature, gas temperature, electron density, etc.). All of these characteristics are of significant influence on dust growth, as was shown in section 5.

The fundamental discharge types are Townsend, corona, glow and arc [108]. The Townsend discharge and corona

discharge are characterized by a localized ionization, which is undesired for the application at hand because they result in a spread in growth conditions and therefore a spread in size distribution. An arc discharge is typically a thermal plasma, leading to high gas temperatures. As discussed in subsection 5.3, temperature is an important control parameter for dust growth. Because of the very sensitive nature of dust production for different temperatures, an arc discharge should be avoided. The glow discharge is characteristically homogeneous and non-LTE, meaning that gas temperature can be tuned independent of the discharge. For the reasons above, a glow discharge is recommended over other types of discharges.

8.2.2 Curvature

The curvature of the electrode surfaces plays a large role in determining the electric field profile in a plasma reactor. Two distinct types of geometries are possible: coaxial (curved) and co-planar (flat). In coaxial geometry (e.g. Figure 8.1b), the electric field near the inner electrode is enhanced relative to the electric field of an equally spaced co-planar (e.g. Figures 8.1a and 8.1c) setup with the same voltage. The local enhanced electric field aids the plasma ignition (i.e. a lower voltage is compared relative to the co-planar setup), but also enables the transition to a more localized plasma mode ($\alpha - \gamma$), which might yield uncontrollable and unpredictable behavior.

Moreover, the electrode curvature also causes a difference in plasma sheath thickness between the two electrodes. If the decrease of the plasma potential to ground potential occurs over a smaller distance, the electric field is consequently higher. A higher electric field on the inner electrode causes higher ion energies bombarding the surface. Even in the precursor-free plasma experiments performed for this work, it was observed that ions could penetrate the Tungsten inner electrode, leading to surface modifications and surface bursting.

For these reasons, it is strongly encouraged that co-axial electrodes are not used.

8.2.3 Shielding

The purpose of adding a dielectric material is historically to limit the current drawn from an electrode. Naturally, that influences the behavior of the plasma. Moreover, a shielded electrode often has reduced sputtering compared to a bare metallic electrode.

The application areas of dust growth and thin film deposition are vastly different, but the reaction environments are largely the same. This means that any device aiming to do one of them will inherently also have the other as a negative side-effect. Scientific literature is aimed mostly at thin film deposition because of its applications in industry, and generally dust growth is viewed as the negative side-effect that should be prevented. The effect that thin film deposition has on a reactor intended for dust production must be considered carefully.

In dust growth devices, thin film coating of the surfaces of the device leads to undesirable consequences. In particular, coating of naked electrodes due to thin film deposition of a dielectric material leads to a reduced surface emission constant, possibly having a significant change on electron density and hence dust production. Moreover, the film thickness is significant relative to the gap width. Both consequences influence the complex impedance of the system, leading to different optimal matching conditions and shorter lifetime of the system. In the experiments performed for this work, it is indeed observed that plasma ignition becomes more difficult when the surface coatings of the electrode increase in thickness leading to poor reproducibility.

Moreover, it is found that adding a dielectric barrier to an electrode prevents a constricted plasma mode from occurring [109]. As this mode is strongly inhomogeneous, it is undesirable that the transition to a constricted mode occurs in a dust reactor.

For all the reasons above, shielded electrodes are deemed superior to bare metal electrodes in the specific case that they are exposed to complex plasmas.

8.2.4 Dimensions

The growth time is determined predominantly by the residence time of flow inside plasma. This parameter is in turn determined by the gas flow, axial length of the plasma volume, and plasma pulse characteristics. As such, the length of the plasma in the flow (axial) direction is one of the critical parameters in determining particle size distribution. It is easier to customize the dust size distribution if the length scale of the plasma is adjustable in addition to the gas flow speed and plasma duty cycle.

The inter-electrode dimension is limited by Paschen's Law, which determines the voltage needed to ignite a plasma. For a reactor at atmospheric pressure, the voltage quickly becomes unattainable for increasing inter-electrode distance. The inter-electrode distances that are used for RF vary from 1 mm [110] to 2 cm [44]. Co-axial electrode configurations have the benefit of having an arbitrary axial length while being limited in the radial direction by Paschen's Law. Co-planar-like electrode configurations are limited in lengths scale but have freedom in the planar dimensions.

Deposition on the reactor walls needs to be taken into account in the design as well. To maximize the ratio between reacting volume versus reactor wall surface area, it is beneficial to have a large off-axial size.

8.3 Precursor mixing

Any surface that is in contact with a reacting precursor must be assumed to get contaminated. The lifetime of a complex plasma is heavily dependent on the jet design [111]. In the experimental setup for this work, the precursor was added to the carrier gas and was in contact with the dielectric barrier of the ground electrode as well as the tungsten RF electrode. As a result, both surfaces were heavily covered by dust or thin films leading to a lifetime of the order of 100 hours.

This can be avoided if the precursor is not present in the bulk plasma, but rather in the plasma effluent (i.e. spatial afterglow). It is suggested that this is the most effective technique of keeping the plasma reactor clean, but it drastically lowers the maximum plasma residence time (if the effluent is not long) and adjustability thereof.

There are various precursor injection concepts used in literature, in addition to the one discussed in section 4. In essence, the central theme of the different concepts is where (relative to the plasma) the precursor is injected. In the case of the experimental setup used for this work (section 4), the precursor is mixed with the carrier gas before it enters the plasma volume. In case of the capillary injection concept (Figure 8.2a), the precursor mixing can be tuned from anywhere between the start of the plasma volume to somewhere in the effluent. The nozzle injection concept and spray injection concept both inject precursor into the plasma effluent.

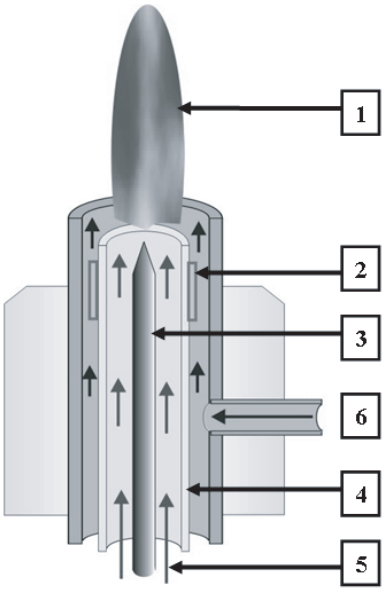

(a) *Capillary jet with nested tubes for additional thin film precursor admixture: (1) Plasma jet, (2) outer grounded ring electrode, (3) inner rf rod electrode, (4) inner quartz capillary, (5) buffer gas channel, (6) precursor channel for carrier gas (N2) with reactive admixture. [112]*

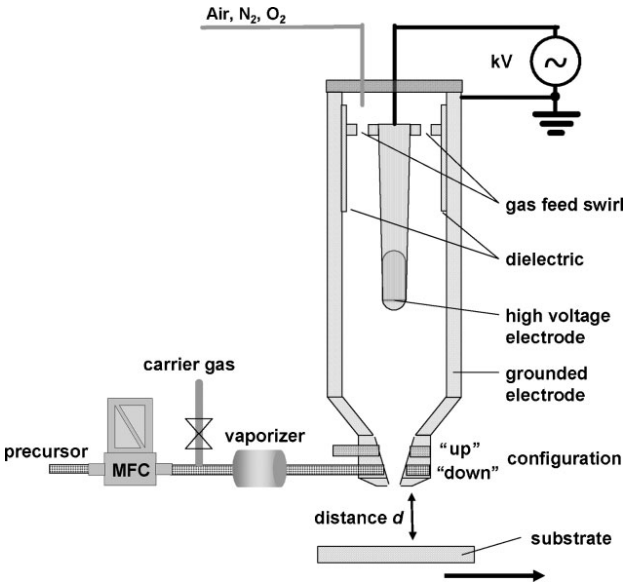

(b) *Nozzle injection concept. [56]*

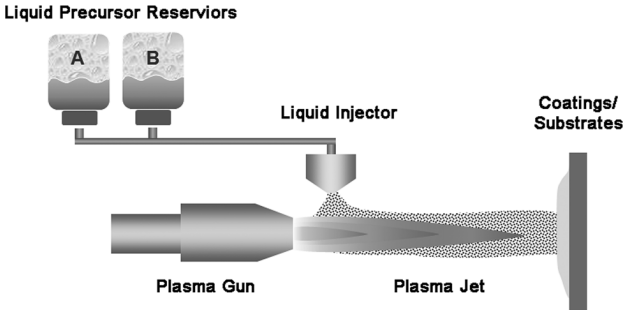

(c) *Liquid spray injector in effluent. [113]*

Figure 8.2: *Various precursor injection concepts.*

8.4 Gas flow geometry

8.4.1 Vortices

Turbulence makes the residence time less uniform and less predictable. To reduce the lowest achievable spread in particle size and to make predictions about particle size distributions more reliable, flow turbulence should be avoided at the design level. Within the jet, this means that precursor should not be injected with a large difference in velocity to the rest of the flow.

In the current proof-of-concept setup, the plasma jet (2mm inner diameter) exits into a large vessel (10cm length scale), inducing high velocity gradients and hence vortices and turbulence. It was observed that these vortices

could re-introduce ‘old’ flow into the spatial afterglow of the plasma.

8.4.2 Heavy particles

In contrast to the small ($\sim$10 nm) particles that are soluble in the carrier gas, the device should be able to produce and transport large ($\sim$1 µm) particles as well. For these particles, gravity dominates motion. If at any point the gas flow is horizontal, heavy particles will drop down and possibly stick to a surface.

It is therefore noted that flow should simply be directed vertically before being integrated with other components in e.g. a testing system.

8.5 Design proposal

Considering all of the above design parameters has lead to the following concept proposal. The author suggests that the proposal below will lead to a device that is optimally suited for dust production. An illustration is shown in Figure 8.3.

Discharge type: It is recommended to use a glow discharge for its cold and homogeneous nature.

Curvature: Axial symmetry is preferred for stimulating a predictable laminar flow, as well as for almost all diagnostical methods. Given that co-axial configurations heavily promote $\alpha - \gamma$ transitions, and γ mode is more localized than α mode, it is advised that the plasma reactor is chosen with a co-radial (double ring) design.

Shielding: The experience during this project with a bare metal electrode exposed to plasma - even without adding a reactive precursor - is that ion bombarding lowers the lifetime of an electrode to tens of hours of exposure. Based on that, it is heavily advised that both electrodes of the plasma reactor are covered with a dielectric barrier.

Dimensions: It is advised to have at least one of the electrodes axially translatable. The plasma volume and electron temperature can then be tuned. This makes the inter-electrode distance arbitrary to define, but a maximum achievable distance of 8 cm is estimated to be more than enough. Ring inner diameters of 6 mm were used successfully in the past to ignite plasma [107]. For a first-time-right design, it is advised that this dimension is adopted. For a research design, it is advised to engineer different sizes of electrodes to experiment with different volume-to-surface ratio's.

Precursor injection: It is proposed that the nozzle injection concept is used, with the nozzle located between the two ring electrodes. This way, the injection location can be tuned to balance residence time and reactor contamination. Relative to the capillary injection method, there is no tube in the plasma that influences the discharge.

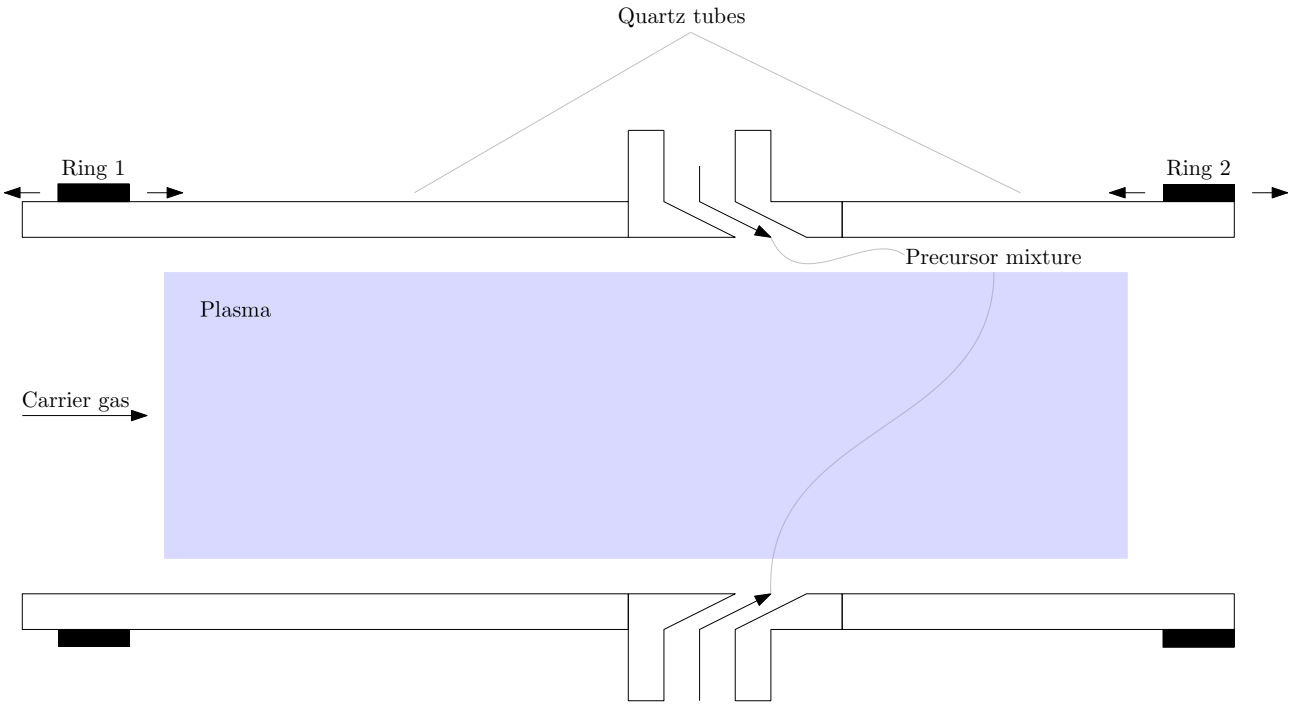

Figure 8.3: *Concept proposal for a dust producing jet.*

9 Acknowledgments

Work in academia is quite different from industry in that it is mostly self-managed. With that additional responsibility comes a steep learning curve. Without the aid of others, climbing that curve would not have been as fruitful and amicable as it was. In this section, I would like to show my gratitude.

First and foremost, I would like to thank my scientific supervisors: Job Beckers, Tim Donders, and Tim Staps. Job, I thank you for your constructive motivation to deliver scientifically sound results. Your supervision during my bachelor's final project, internship, and now my master's graduation project have all been stimulating. The conversations on life after study have also been fascinating and I am positive that this has not been our latest collaboration. Tim, your endless positivity continues to amaze me. Your support has always been encouraging, and I value our efforts to make this a mutual collaboration greatly. May we have a lot more coffee talks and boulder sessions! Other Tim, the same holds for you. Additionally, your sharp and analytical thought process is admirable. Thank you for the numerous conversations we had on my career and the independent stance you took in them. I am grateful for arranging the opportunity for this work at Prodrive.

Niels Smith, thank you for the supervision and representing the Prodrive Technologies stake. You have helped me consider the 'development' consequences in a project where it is easy to be lost in research. I enjoyed our talkative lunch walks and diners, discussing personal matters in an openness I do not share with many. Wessel van Dijk, I thank you for mediating between me and Prodrive in a project where I imagine that has been harder than in most. Your efforts to help me find a fit in Prodrive are greatly appreciated! Bram Looman, even though our collaboration was short-lived, I thank you for your honest interest and enthusiasm towards my work.

I thank the members of the graduation committee, Jan van Dijk and Henk Huinink, for taking the time to read this thesis and devising intriguing lines of attack for my defense.

Ab en Pieter, thank you for your skillful assistance and support of all activities in the lab. Moreover, thanks for the cheerful contributions to certain areas on the 3rd and 6th floor. To all of the EPG group, but in particular, Patrick, Federico, Guido, Saman, and Judith, thank you for the almost-200 lunch walks. Discussions on whether or not purple is a color, the composition of peppermints and 'taste' of menthol, and the relatedness of pickles to cucumbers will not be forgotten. Let us call it 'universal curiosity'...

Lennart, my mentor, as I have said many times before: the personal lessons I have learned from you have been invaluable. I could not have climbed the metaphorical hill with this result without your guidance, and I predict your influence will be of exponential contribution to me both personally and professionally.

Amber, thank you for your endless support during my studies. Our hugs and giggles have far outweighed the pitfalls that I encountered this past year. Mick, thank you for the weekly meet-ups. Our chess matches, bold ambition, and creativity are things I cherish dearly. Swen, Jelle, Dennis, Ruud, Sil: it has been an honor to have lived longer with you as friends than without. Philosophical debate or snowball fight, every activity is due when I can do it with you. Giel, Stan, the entertainment in the past years has been hilarious, even when it resulted in choking on vanilla pudding.

I thank my parents and brother for their continued support over the years, both in good times and in great times. For everyone whom I may have forgotten to thank implicitly or explicitly: thanks, I appreciate it!

Martijn

References

1. Pachauri, R. K. *et al. Climate change 2014: synthesis report. Contribution of Working Groups I, II and III to the fifth assessment report of the Intergovernmental Panel on Climate Change* (IPCC, 2014).
2. Jiang, J., Ye, B. & Liu, J. Research on the peak of CO2 emissions in the developing world: Current progress and future prospect. *Applied Energy* **235,** 186–203. https://doi.org/10.1016/j.apenergy.2018.10.089 (Feb. 2019).
3. Schlesinger, M. E. & Mitchell, J. F. B. Climate model simulations of the equilibrium climatic response to increased carbon dioxide. *Reviews of Geophysics* **25,** 760. https://doi.org/10.1029/rg025i004p00760 (1987).
4. Christidis, N., Hurley, M. D., Pinnock, S., Shine, K. P. & Wallington, T. J. Radiative forcing of climate change by CFC-11 and possible CFC replacements. *Journal of Geophysical Research: Atmospheres* **102,** 19597–19609. https://doi.org/10.1029/97jd01137 (Aug. 1997).
5. Grewe, V., Dahlmann, K., Matthes, S. & Steinbrecht, W. Attributing ozone to NOx emissions: Implications for climate mitigation measures. *Atmospheric Environment* **59,** 102–107. https://doi.org/10.1016/j.atmosenv.2012.05.002 (Nov. 2012).
6. Cesaroni, G. *et al.* Long term exposure to ambient air pollution and incidence of acute coronary events: prospective cohort study and meta-analysis in 11 European cohorts from the ESCAPE Project. *BMJ* **348,** f7412–f7412. https://doi.org/10.1136/bmj.f7412 (Jan. 2014).
7. Hoek, G. *et al.* Long-term air pollution exposure and cardio- respiratory mortality: a review. *Environmental Health* **12.** https://doi.org/10.1186/1476-069x-12-43 (May 2013).
8. Bourdrel, T., Bind, M.-A., Béjot, Y., Morel, O. & Argacha, J.-F. Cardiovascular effects of air pollution. *Archives of Cardiovascular Diseases* **110,** 634–642. https://doi.org/10.1016/j.acvd.2017.05.003 (Nov. 2017).
9. Hamra, G. B. *et al.* Outdoor Particulate Matter Exposure and Lung Cancer: A Systematic Review and Meta-Analysis. *Environmental Health Perspectives.* https://doi.org/10.1289/ehp.1408092 (June 2014).
10. Ciabattini, M., Rizzello, E., Lucaroni, F., Palombi, L. & Boffetta, P. Systematic review and meta-analysis of recent high-quality studies on exposure to particulate matter and risk of lung cancer. *Environmental Research,* 110440. https://doi.org/10.1016/j.envres.2020.110440 (Nov. 2020).
11. Wang, K., Hao, Y., Au, W., Christiani, D. C. & Xia, Z.-L. A Systematic Review and Meta-Analysis on Short-Term Particulate Matter Exposure and Chronic Obstructive Pulmonary Disease Hospitalizations in China. *Journal of Occupational & Environmental Medicine* **61,** e112–e124. https://doi.org/10.1097/jom.0000000000001539 (Apr. 2019).
12. Shah, A. S. V. *et al.* Short term exposure to air pollution and stroke: systematic review and meta-analysis. *BMJ,* h1295. https://doi.org/10.1136/bmj.h1295 (Mar. 2015).
13. *Particle size analysis — Laser diffraction methods* Standard (International Organization for Standardization, Geneva, CH, Jan. 2020).
14. Bai, Y. *et al.* Washable Multilayer Triboelectric Air Filter for Efficient Particulate Matter PM2.5Removal. *Advanced Functional Materials* **28,** 1706680. https://doi.org/10.1002/adfm.201706680 (Feb. 2018).
15. Zhang, R. *et al.* Nanofiber Air Filters with High-Temperature Stability for Efficient PM2.5 Removal from the Pollution Sources. *Nano Letters* **16,** 3642–3649. https://doi.org/10.1021/acs.nanolett.6b00771 (May 2016).
16. Ohlwein, S., Kappeler, R., Joss, M. K., Künzli, N. & Hoffmann, B. Health effects of ultrafine particles: a systematic literature review update of epidemiological evidence. *International Journal of Public Health* **64,** 547–559. https://doi.org/10.1007/s00038-019-01202-7 (Feb. 2019).
17. Health Effects Institute. *Understanding the Health Effects of Ambient Ultrafine Particles* https://www.healtheffects.org/publication/understanding-health-effects-ambient-ultrafine-particles (2022).
18. Wolf, K. *et al.* Associations between short-term exposure to particulate matter and ultrafine particles and myocardial infarction in Augsburg, Germany. *International Journal of Hygiene and Environmental Health* **218,** 535–542. https://doi.org/10.1016/j.ijheh.2015.05.002 (Aug. 2015).

19. Dhawan, S. *et al.* Enhancing charging and capture efficiency of aerosol nanoparticles using an atmospheric-pressure, flow-through RF plasma with a downstream DC bias. *Aerosol Science and Technology* **54,** 1249–1254. https://doi.org/10.1080/02786826.2020.1807459 (Aug. 2020).
20. Djarek Hendrikus Josephus Maria van den Hoogen Timmy Jacobus Adrianus Staps, K. S. S. US10890519B2. https://patents.google.com/patent/WO2017220618A1(2016).
21. *Road vehicles — Test contaminants for filter evaluation — Part 1: Arizona test dust* Standard (International Organization for Standardization, Geneva, CH, Mar. 2016).
22. *RM 8632 - Ultra Fine Test Dust (UFTD)* https://www-s.nist.gov/srmors/view_detail.cfm?srm=8632 (2021).
23. Merck KGaA. *Silica nanoparticles* https://www.sigmaaldrich.com/NL/en/product/aldrich/914843 (2022).
24. microParticles GmbH. *Silica particles (SiO2-R) in the size range 150 nm – 25 µm* https://www.microparticles-shop.de/Monodisperse-Particles-for-Research-Purposes/Silica-particles-SiO2-R-in-the-size-range-150-nm-25-m:::1_6.html?language=en (2022).
25. Palas GmbH. *LSPG 16890 Aerosol generator* https://www.palas.de/en/product/lspg16890 (2022).
26. Bouchoule, A., Plain, A., Boufendi, L., Blondeau, J. P. & Laure, C. Particle generation and behavior in a silane-argon low-pressure discharge under continuous or pulsed radio-frequency excitation. *Journal of Applied Physics* **70,** 1991–2000. https://doi.org/10.1063/1.349484 (Aug. 1991).
27. Belmonte, T., Henrion, G. & Gries, T. Nonequilibrium Atmospheric Plasma Deposition. *Journal of Thermal Spray Technology* **20,** 744–759. https://doi.org/10.1007/s11666-011-9642-0 (Mar. 2011).
28. Steves, S. *Barrier coating and sterilization of plastics by microwave and radio frequency low-pressure plasmas* doctoralthesis (Ruhr-Universität Bochum, Universitätsbibliothek, 2013).
29. Premkumar, P. A. *et al.* High Quality SiO2-like Layers by Large Area Atmospheric Pressure Plasma Enhanced CVD: Deposition Process Studies by Surface Analysis. *Plasma Processes and Polymers* **6,** 693–702. https://doi.org/10.1002/ppap.200900033 (Oct. 2009).
30. Benedikt, J., Raballand, V., Yanguas-Gil, A., Focke, K. & von Keudell, A. Thin film deposition by means of atmospheric pressure microplasma jet. *Plasma Physics and Controlled Fusion* **49,** B419–B427. https://doi.org/10.1088/0741-3335/49/12b/s39 (Nov. 2007).
31. Morent, R. *et al.* Organic–inorganic behaviour of HMDSO films plasma-polymerized at atmospheric pressure. *Surface and Coatings Technology* **203,** 1366–1372. https://doi.org/10.1016/j.surfcoat.2008.11.008 (Feb. 2009).
32. Landreau, X. *et al.* Effects of the substrate temperature on the deposition of thin SiOx films by atmospheric pressure microwave plasma torch (TIA). *Surface and Coatings Technology* **205,** S335–S341. https://doi.org/10.1016/j.surfcoat.2011.03.123 (July 2011).
33. Sterling, H. & Swann, R. Chemical vapour deposition promoted by r.f. discharge. *Solid-State Electronics* **8,** 653–654. https://doi.org/10.1016/0038-1101(65)90033-x (Aug. 1965).
34. Bouchoule, A. & Boufendi, L. Particulate formation and dusty plasma behaviour in argon-silane RF discharge. *Plasma Sources Science and Technology* **2,** 204–213. https://doi.org/10.1088/0963-0252/2/3/011 (Aug. 1993).
35. Kortshagen, U. & Bhandarkar, U. Modeling of particulate coagulation in low pressure plasmas. *Physical Review E* **60,** 887–898. https://doi.org/10.1103/physreve.60.887 (July 1999).
36. Boufendi, L. & Bouchoule, A. Particle nucleation and growth in a low-pressure argon-silane discharge. *Plasma Sources Science and Technology* **3,** 262–267. https://doi.org/10.1088/0963-0252/3/3/004 (Aug. 1994).
37. Stoffels, E., Stoffels, W. W., Kroesen, G. M. W. & de Hoog, F. J. Dust formation and charging in an Ar/SiH4 radio-frequency discharge. *Journal of Vacuum Science & Technology A: Vacuum, Surfaces, and Films* **14,** 556–561. https://doi.org/10.1116/1.580144 (Mar. 1996).
38. Stoffels, E., Stoffels, W. W., Kersten, H., Swinkels, G. H. P. M. & Kroesen, G. M. W. Surface Processes of Dust Particles in Low Pressure Plasmas. *Physica Scripta* **T89,** 168. https://doi.org/10.1238/physica.topical.089a00168 (2001).
39. Kroesen, G. M. W. *et al.* Negative ions and particle formation in low-pressure halocarbon discharges. *Plasma Sources Science and Technology* **3,** 246–251. https://doi.org/10.1088/0963-0252/3/3/002 (Aug. 1994).

40. Beckers, J. & Kroesen, G. M. W. Surprising temperature dependence of the dust particle growth rate in low pressure Ar/C2H2 plasmas. *Applied Physics Letters* **99,** 181503. https://doi.org/10.1063/1.3658730 (Oct. 2011).

41. Beckers, J. & Kroesen, G. M. W. Gas temperature dependence of coagulation onset times for nanoparticles in low pressure hydrocarbon plasmas. *Applied Physics Letters* **103,** 123106. https://doi.org/10.1063/1.4821449 (Sept. 2013).

42. Sorokin, M., Kroesen, G. & Stoffels, W. Temperature Dependence and Silane Consumption During Particle Formation in Ar–Silane RF Capacitively Coupled Plasma. *IEEE Transactions on Plasma Science* **32,** 731–737. https://doi.org/10.1109/tps.2004.826137 (Apr. 2004).

43. Wallimann, R., Roth, C. & von Rohr, P. R. Nanoparticle production from HMDSO in atmospheric pressure argon-oxygen plasma. *Plasma Processes and Polymers* **15,** 1700202. https://doi.org/10.1002/ppap.201700202 (Mar. 2018).

44. Abuyazid, N. H. *et al.* Understanding the depletion of electrons in dusty plasmas at atmospheric pressure. *Plasma Sources Science and Technology* **29,** 075011. https://doi.org/10.1088/1361-6595/ab9cc3 (July 2020).

45. Bonilla, J. S. G. *et al.* Improvement of polymer properties for powder bed fusion by combining in situ PECVD nanoparticle synthesis and dry coating. *Plasma Processes and Polymers* **18,** 2000247. https://doi.org/10.1002/ppap.202000247 (Feb. 2021).

46. Kramer, N. J., Aydil, E. S. & Kortshagen, U. R. Requirements for plasma synthesis of nanocrystals at atmospheric pressures. *Journal of Physics D: Applied Physics* **48,** 035205. https://doi.org/10.1088/0022-3727/48/3/035205 (Jan. 2015).

47. On the Effects of Atomic Radiation, U. N. S. C. *Sources and Effects of Ionizing Radiation: Sources* ISBN: 978-92-1-142274-0 (United Nations Publications, 2010).

48. Hofmann, S., van Gessel, A. F. H., Verreycken, T. & Bruggeman, P. Power dissipation, gas temperatures and electron densities of cold atmospheric pressure helium and argon RF plasma jets. *Plasma Sources Science and Technology* **20,** 065010. https://doi.org/10.1088/0963-0252/20/6/065010 (Nov. 2011).

49. Van Gessel, B., Brandenburg, R. & Bruggeman, P. Electron properties and air mixing in radio frequency driven argon plasma jets at atmospheric pressure. *Applied Physics Letters* **103,** 064103. https://doi.org/10.1063/1.4817936 (Aug. 2013).

50. Balcon, N., Aanesland, A. & Boswell, R. Pulsed RF discharges, glow and filamentary mode at atmospheric pressure in argon. *Plasma Sources Science and Technology* **16,** 217–225. https://doi.org/10.1088/0963-0252/16/2/002 (Jan. 2007).

51. Grill, A. *Cold Plasma Materials Fabrication* ISBN: 978-0-780-34714-4 (Wiley-IEEE Press, Mar. 1994).

52. Pankaj, S., Wan, Z. & Keener, K. Effects of Cold Plasma on Food Quality: A Review. *Foods* **7,** 4. https://doi.org/10.3390%2Ffoods7010004 (Jan. 2018).

53. Laroussi, M. Cold Plasma in Medicine and Healthcare: The New Frontier in Low Temperature Plasma Applications. *Frontiers in Physics* **8.** https://doi.org/10.3389%2Ffphy.2020.00074 (Mar. 2020).

54. Shukla, P. & Mamun, A. *Introduction to Dusty Plasma Physics* ISBN: 9781420034103 (CRC Press, Apr. 2015).

55. Hegemann, D., Vohrer, U., Oehr, C. & Riedel, R. Deposition of SiOx films from O2/HMDSO plasmas. *Surface and Coatings Technology* **116-119,** 1033–1036. https://doi.org/10.1016/s0257-8972(99)00092-4 (Sept. 1999).

56. Lommatzsch, U. & Ihde, J. Plasma Polymerization of HMDSO with an Atmospheric Pressure Plasma Jet for Corrosion Protection of Aluminum and Low-Adhesion Surfaces. *Plasma Processes and Polymers* **6,** 642–648. https://doi.org/10.1002/ppap.200900032 (Oct. 2009).

57. Jeckell, Z. *et al.* Silicon Dioxide Deposited Using Atmospheric Pressure Plasma Chemical Vapor Deposition for Improved Adhesion and Water Intrusion Resistance for Lightweight Manufacturing. *Surfaces and Interfaces* **23,** 100989. https://doi.org/10.1016/j.surfin.2021.100989 (Apr. 2021).

58. Wetering, F. V. D. *Formation and dynamics of nanoparticles in plasmas* 2016. https://research.tue.nl/en/publications/formation-and-dynamics-of-nanoparticles-in-plasmas(f3331ca8-0d98-4cf4-92cb-58a6a8ca047c).html.

59. Bouchoule, A. *Dusty Plasmas* ISBN: 0471973866 (Wiley-Blackwell, Aug. 1999).

60. Despax, B., Gaboriau, F., Caquineau, H. & Makasheva, K. Influence of the temporal variations of plasma composition on the cyclic formation of dust in hexamethyldisiloxane-argon radiofrequency discharges: Analysis by time-resolved mass spectrometry. *AIP Advances* **6,** 105111. https://doi.org/10.1063/1.4966254 (Oct. 2016).

61. Alexander, M. R., Jones, F. R. & Short, R. D. Mass Spectral Investigation of the Radio-Frequency Plasma Deposition of Hexamethyldisiloxane. *The Journal of Physical Chemistry B* **101,** 3614–3619. https://doi.org/10.1021/jp970663b (May 1997).

62. Basner, R., Foest, R., Schmidt, M., Becker, K. & Deutsch, H. Absolute total and partial electron impact ionization cross sections of hexamethyldisiloxane. *International Journal of Mass Spectrometry* **176,** 245–252. https://doi.org/10.1016/s1387-3806(98)14027-7 (July 1998).

63. Lamendola, R., d'Agostino, R. & Fracassi, F. Thin film deposition from hexamethyldisiloxane fed glow discharges. *Plasmas and Polymers* **2,** 147–164. https://doi.org/10.1007/bf02766151 (Sept. 1997).

64. Hegemann, D., Brunner, H. & Oehr, C. Deposition rate and three-dimensional uniformity of RF plasma deposited SiOx films. *Surface and Coatings Technology* **142-144,** 849–855. https://doi.org/10.1016/s0257-8972(01)01100-8 (July 2001).

65. Reuter, R., Ellerweg, D., von Keudell, A. & Benedikt, J. Surface reactions as carbon removal mechanism in deposition of silicon dioxide films at atmospheric pressure. *Applied Physics Letters* **98,** 111502. https://doi.org/10.1063/1.3565965 (Mar. 2011).

66. Friedrich, J. Mechanisms of Plasma Polymerization - Reviewed from a Chemical Point of View. *Plasma Processes and Polymers* **8,** 783–802. https://doi.org/10.1002/ppap.201100038 (July 2011).

67. Bleecker, K. D., Bogaerts, A. & Goedheer, W. Detailed modeling of hydrocarbon nanoparticle nucleation in acetylene discharges. *Physical Review E* **73.** https://doi.org/10.1103/physreve.73.026405 (Feb. 2006).

68. Yasuda, H. & Hirotsu, T. Critical evaluation of conditions of plasma polymerization. *Journal of Polymer Science: Polymer Chemistry Edition* **16,** 743–759. https://doi.org/10.1002/pol.1978.170160403 (Apr. 1978).

69. Magni, D., Deschenaux, C., Hollenstein, C., Creatore, A. & Fayet, P. Oxygen diluted hexamethyldisiloxane plasmas investigated by means ofin situinfrared absorption spectroscopy and mass spectrometry. *Journal of Physics D: Applied Physics* **34,** 87–94. https://doi.org/10.1088/0022-3727/34/1/315 (Dec. 2000).

70. Wavhal, D. S., Zhang, J., Steen, M. L. & Fisher, E. R. Investigation of Gas Phase Species and Deposition of SiO2 Films from HMDSO/O2 Plasmas. *Plasma Processes and Polymers* **3,** 276–287. https://doi.org/10.1002/ppap.200500140 (Apr. 2006).

71. Seigneur, C. *et al.* Simulation of Aerosol Dynamics: A Comparative Review of Mathematical Models. *Aerosol Science and Technology* **5,** 205–222. https://doi.org/10.1080/02786828608959088 (Jan. 1986).

72. Allen, J. E. Probe theory - the orbital motion approach. *Physica Scripta* **45,** 497–503. https://doi.org/10.1088/0031-8949/45/5/013 (May 1992).

73. Gatti, M. & Kortshagen, U. Analytical model of particle charging in plasmas over a wide range of collisionality. *Physical Review E* **78.** https://doi.org/10.1103/physreve.78.046402 (Oct. 2008).

74. Santos, B., Cacot, L., Boucher, C. & Vidal, F. Electrostatic enhancement factor for the coagulation of silicon nanoparticles in low-temperature plasmas. *Plasma Sources Science and Technology* **28,** 045002. https://doi.org/10.1088/1361-6595/ab0a2b (Apr. 2019).

75. Galli, F. & Kortshagen, U. R. Charging, Coagulation, and Heating Model of Nanoparticles in a Low-Pressure Plasma Accounting for Ion–Neutral Collisions. *IEEE Transactions on Plasma Science* **38,** 803–809. https://doi.org/10.1109/tps.2009.2035700 (Apr. 2010).

76. Bohren, C. F. & Huffman, D. R. *Absorption and Scattering of Light by Small Particles* ISBN: 9780471293408 (Wiley-VCH, 1983).

77. Verhoeven, J. W. Glossary of terms used in photochemistry (IUPAC Recommendations 1996). *Pure and Applied Chemistry* **68,** 2223–2286. https://doi.org/10.1351/pac199668122223 (Jan. 1996).

78. Zajíčková, L. *et al.* Plasma modification of polycarbonates. *Surface and Coatings Technology* **142-144,** 449–454. https://doi.org/10.1016/s0257-8972(01)01134-3 (July 2001).

79. *Optical constants of SiO2 (Silicon dioxide, Silica, Quartz)* https://refractiveindex.info/?shelf=main&book=SiO2&page=Rodriguez-de_Marcos (2022).

80. *Optical constants of (C2H6OSi)n (Polydimethylsiloxane, PDMS)* https://refractiveindex.info/?shelf=organic&book=polydimethylsiloxane&page=Gupta (2022).

81. Saloum, S. & Naddaf, M. Optical constants of silicone-like (Si:Ox:Cy:Hz) thin films deposited on quartz using hexamethyldisiloxane in a remote RF hollow cathode discharge plasma. *Vacuum* **82,** 50–55. https://doi.org/10.1016/j.vacuum.2007.03.007 (Sept. 2007).

82. Saloum, S., Naddaf, M. & Alkhaled, B. Properties of thin films deposited from HMDSO/O2 induced remote plasma: Effect of oxygen fraction. *Vacuum* **82,** 742–747. https://doi.org/10.1016/j.vacuum.2007.10.009 (Apr. 2008).

83. Mota, R. P. *et al.* HMDSO plasma polymerization and thin film optical properties. *Thin Solid Films* **270,** 109–113. https://doi.org/10.1016/0040-6090(95)06938-0 (Dec. 1995).

84. Alexandrov, S. E., McSporran, N. & Hitchman, M. L. Remote AP-PECVD of Silicon Dioxide Films from Hexamethyldisiloxane (HMDSO). *Chemical Vapor Deposition* **11,** 481–490. https://doi.org/10.1002/cvde.200506385 (Dec. 2005).

85. Schäfer, J. *MatScat* https://www.mathworks.com/matlabcentral/fileexchange/36831-matscat (2022).

86. Onofri, F., Ren, K. & Grisolia, C. Development of an in situ ITER dust diagnostic based on extinction spectrometry: Dedicated light scattering models. *Journal of Nuclear Materials* **390-391,** 1093–1096. https://doi.org/10.1016/j.jnucmat.2009.01.272 (June 2009).

87. Ligon, D. A., Gillespie, J. B. & Pellegrino, P. Aerosol properties from spectral extinction and backscatter estimated by an inverse Monte Carlo method. *Applied Optics* **39,** 4402. https://doi.org/10.1364/ao.39.004402 (Aug. 2000).

88. Dap, S., Lacroix, D., Hugon, R. & Bougdira, J. Retrieving particle size and density from extinction measurement in dusty plasma, Monte Carlo inversion and Ray-tracing comparison. *Journal of Quantitative Spectroscopy and Radiative Transfer* **128,** 18–26. https://doi.org/10.1016/j.jqsrt.2012.07.010 (Oct. 2013).

89. Lawson, C. L. & Hanson, R. J. *Solving Least Squares Problems* ISBN: 9781611971217 (SIAM, Nov. 1995).

90. Beijer, P. A. C., Sobota, A., van Veldhuizen, E. M. & Kroesen, G. M. W. Multiplying probe for accurate power measurements on an RF driven atmospheric pressure plasma jet applied to the COST reference microplasma jet. *Journal of Physics D: Applied Physics* **49,** 104001. https://doi.org/10.1088/0022-3727/49/10/104001 (Feb. 2016).

91. Schulze, J., Heil, B. G., Luggenhölscher, D., Brinkmann, R. P. & Czarnetzki, U. Stochastic heating in asymmetric capacitively coupled RF discharges. *Journal of Physics D: Applied Physics* **41,** 195212. https://doi.org/10.1088/0022-3727/41/19/195212 (Sept. 2008).

92. Platier, B., Staps, T. J. A., Hak, C. C. J. M., Beckers, J. & IJzerman, W. L. Resonant microwaves probing acoustic waves from an RF plasma jet. *Plasma Sources Science and Technology* **29,** 045024. https://doi.org/10.1088/1361-6595/ab7d8e (Apr. 2020).

93. Staps, T. *Towards experimental characterization of nanoparticle charging in plasmas* English. Proefschrift. PhD thesis (Applied Physics, Feb. 2022). ISBN: 978-90-386-5439-3.

94. Singh, K. P. & Roy, S. Impedance matching for an asymmetric dielectric barrier discharge plasma actuator. *Applied Physics Letters* **91,** 081504. https://doi.org/10.1063/1.2773932 (Aug. 2007).

95. Raoult, F.-M. Recherches expérimentales sur les tensions de vapeur des dissolutions. *Journal de Physique Théorique et Appliquée* **8,** 5–20. https://doi.org/10.1051/jphystap:0188900800500 (1889).

96. Scott, D. W. *et al.* Hexamethyldisiloxane: chemical thermodynamic properties and internal rotation about the siloxane linkage. *The Journal of Physical Chemistry* **65,** 1320–1326. https://doi.org/10.1021/j100826a010 (Aug. 1961).

97. Babayan, S. E. *et al.* Deposition of silicon dioxide films with a non-equilibrium atmospheric-pressure plasma jet. *Plasma Sources Science and Technology* **10,** 573–578. https://doi.org/10.1088/0963-0252/10/4/305 (Sept. 2001).

98. Fridman, A. A., Boufendi, L., Hbid, T., Potapkin, B. V. & Bouchoule, A. Dusty plasma formation: Physics and critical phenomena. Theoretical approach. *Journal of Applied Physics* **79,** 1303–1314. https://doi.org/10.1063%2F1.361026 (Feb. 1996).

99. Staps, T. J. A., Donders, T. J. M., Platier, B. & Beckers, J. In-situ measurement of dust charge density in nanodusty plasma. *Journal of Physics D: Applied Physics* **55,** 08LT01. https://doi.org/10.1088%2F1361-6463%2Fac3581 (Nov. 2021).

100. Stoffels, W. W., Stoffels, E., Swinkels, G. H. P. M., Boufnichel, M. & Kroesen, G. M. W. Etching a single micrometer-size particle in a plasma. *Physical Review E* **59,** 2302–2304. https://doi.org/10.1103/physreve.59.2302 (Feb. 1999).

101. Greiner, F. *et al.* Diagnostics and characterization of nanodust and nanodusty plasmas. *The European Physical Journal D* **72.** https://doi.org/10.1140/epjd/e2017-80400-7 (May 2018).

102. Boufendi, L., Bouchoule, A. & Hbid, T. Electrical characterization and modeling of a dust forming plasma in a radio frequency discharge. *Journal of Vacuum Science & Technology A: Vacuum, Surfaces, and Films* **14,** 572–576. https://doi.org/10.1116/1.580147 (Mar. 1996).

103. Malyshev, M. V. & Donnelly, V. M. Trace rare gases optical emission spectroscopy: Nonintrusive method for measuring electron temperatures in low-pressure, low-temperature plasmas. *Physical Review E* **60,** 6016–6029. https://doi.org/10.1103/physreve.60.6016 (Nov. 1999).

104. Massines, F., Gherardi, N., Fornelli, A. & Martin, S. Atmospheric pressure plasma deposition of thin films by Townsend dielectric barrier discharge. *Surface and Coatings Technology* **200,** 1855–1861. https://doi.org/10.1016%2Fj.surfcoat.2005.08.010 (Nov. 2005).

105. Golda, J. *et al.* Concepts and characteristics of the 'COST Reference Microplasma Jet'. *Journal of Physics D: Applied Physics* **49,** 084003. https://doi.org/10.1088/0022-3727/49/8/084003 (Jan. 2016).

106. Reuter, S., von Woedtke, T. & Weltmann, K.-D. The kINPen—a review on physics and chemistry of the atmospheric pressure plasma jet and its applications. *Journal of Physics D: Applied Physics* **51,** 233001. https://doi.org/10.1088/1361-6463/aab3ad (May 2018).

107. Schäfer, J., Foest, R., Quade, A., Ohl, A. & Weltmann, K.-D. Local deposition of SiOxplasma polymer films by a miniaturized atmospheric pressure plasma jet (APPJ). *Journal of Physics D: Applied Physics* **41,** 194010. https://doi.org/10.1088/0022-3727/41/19/194010 (Sept. 2008).

108. Lieberman, M. A. & Lichtenberg, A. J. *Principles of Plasma Discharges and Materials Processing* ISBN: 9780471720010 (Wiley-Interscience, Mar. 2005).

109. Shi, J. J., Liu, D. W. & Kong, M. G. Mitigating plasma constriction using dielectric barriers in radio-frequency atmospheric pressure glow discharges. *Applied Physics Letters* **90,** 031505. https://doi.org/10.1063/1.2432233 (Jan. 2007).

110. Golda, J., Kogelheide, F., Awakowicz, P. & der Gathen, V. S.-v. Dissipated electrical power and electron density in an RF atmospheric pressure helium plasma jet. *Plasma Sources Science and Technology* **28,** 095023. https://doi.org/10.1088/1361-6595/ab393d (Sept. 2019).

111. Reuter, R. *et al.* The Role of Oxygen and Surface Reactions in the Deposition of Silicon Oxide like Films from HMDSO at Atmospheric Pressure. *Plasma Processes and Polymers* **9,** 1116–1124. https://doi.org/10.1002%2Fppap.201100146 (Jan. 2012).

112. Foest, R. *et al.* RF Capillary Jet - a Tool for Localized Surface Treatment. *Contributions to Plasma Physics* **47,** 119–128. https://doi.org/10.1002/ctpp.200710017 (Feb. 2007).

113. Jordan, E. H., Jiang, C. & Gell, M. The Solution Precursor Plasma Spray (SPPS) Process: A Review with Energy Considerations. *Journal of Thermal Spray Technology* **24,** 1153–1165. https://doi.org/10.1007/s11666-015-0272-9 (July 2015).